Numerical Investigation of Natural Gas Hydrate Agglomeration and Deposition in High Water Cut Pipeline Systems

Kristine Blænes Gangsøy
University of Bergen, Department of Physics and Technology
Bergen, Norway

June 5, 2018

A thesis in partial fulfilment of the requirements for the degree of *Master of science* in the subject of Process Technology: Multiphase Systems

Acknowledgements

First and foremost I would like to thank my supervisor Prof. Pawel Jan Kosinski for his helpful, always positive and uplifting attitude through the work of this thesis. I appreciate that he always makes me feel welcome at his office, and his ability to explain advanced thing in an uncomplicated way. I am very grateful for the good guidance throughout the work of this thesis.

I would like to express my appreciation to my co-supervisor Prof. Boris Balakin for being curious, critical and most of all helpful. His contribution with knowledge of gas hydrates and the computational fluid dynamics program, STAR CCM+ has been priceless. I am very grateful for all I have learned.

I would also like to thank Prof. Vladimir A. Istomin from SkolTech for help with the literature study. He provided me the Russian articles.

Furthermore, I would like to thank Kjetil Heitmann for computer help. He made it possible to run the simulations faster, by running many more cores in parallel on a computer with greater capacity, relative to the standard student computers at the office.

Finally, I would like to thank my fellow students at my office, Melodía Lucas Pérez and Claus Mevik, that motivated me through this work, and that I could share ups and downs with.

Bergen, June 2018

Kristine Blænes Gangsøy

Abstract

The phenomena of gas hydrate plugging constitute a well known problem in the petroleum production and transport industries. Nevertheless, this issue is still not fully understood, especially for high water cut systems. For mature petroleum fields the amount of water produced increases, which results in increased risk of gas hydrate plug formation in pipelines. From previous work, it is not clear which mechanism is the most dominant for hydrate plug formation in water dominated pipeline systems: increased hydrate slurry viscosity or deposition on the pipeline wall. Knowledge of the mechanism leading to plugging is crucial to obtain efficient and economical risk management strategies for preventing pipeline plugging in such systems in the future.

Computational fluid dynamics (CFD) with the discrete element method (DEM), which is an extension of the Lagrangian modelling methodology, was used to examine the flow of gas, hydrates and water in a pipeline. There is a lack of knowledge regarding interactions forces for naturally occurring gas hydrates in previous numerical works. These are key parameters when investigating hydrate agglomeration and deposition. The hydrate-hydrate cohesion force and the hydrate-wall adhesion force have been found from empirical estimates for model hydrates or regarded as unknown in earlier works. The first part of this thesis therefore focuses on finding better estimates for naturally occurring hydrate interaction from experimental findings. By numerical simulations, the corresponding work of cohesion between hydrate particles was found to be W_{coh} = 7.0 mJ/m^2 and the corresponding work of adhesion to the steel wall material was found to be W_{adh} = 0.8 mJ/m^2.

Furthermore, two different two-dimensional flow systems for investigating the flow were simulated, the fist simulates a stirred tank system, referred to as case 1 and and the second a industrial pipe, referred to as case 2. In case 1, hydrates accumulated at the upper part of the pipe, close to the gas-water interphase, and agglomerates of a wide range of sizes were formed. In case 2, a major hydrate agglomerate was formed in the middle of the pipe. No particle deposition was observed in the simulations due to the shear force from the water phase being too high to allow the particles to adhere to the wall. According to these results, the most probable main mechanism for hydrate plugging in the water phase seems to be hydrate bed formation increasing the hydrate-water slurry viscosity.

Nomenclature

Abbreviations

AAs	Anti-agglomerates
Al	Duralumin
CFD	Computational fluid dynamics
CS	Carbon steel
DEM	Discrete element method
DMT	Derjaguin-Muller-Toporov
DPM	Discrete parcel method
E-E	Eulerian-Eulerian
E-L	Eulerian-Lagrange
F-12	Freon-12
Fl	Fluoroplastic
H	Hydrate
HC	Hydrocarbon
JKR	Johnson-Kendall-Roberts
KHIs	Kinetic hydrate inhibitors
L-J	Lennard-Jones
LDHIs	Low dosage hydrate inhibitors
MMF	Micro mechanical force
P	Pull-off
P-T	Pressure-temperature
PBC	Periodic boundary condition

PTFE	Polytetrafluoretylen
RANS	Reynold-averaged Navier-Stokes
S	Shear
SH	Hydrate structure H
SI	Hydrate structure I
SII	Hydrate structure II
T-F	Two-fluid
THF	Tetrahydrofuran
THIs	Thermodynamic hydrate inhibitors
V/L	Vapour/liquid

Greek Symbols

$\boldsymbol{\tau^t}$	Turbulent stress tensor working on the fluid element	[N/m^2]
$\boldsymbol{\tau}$	Molecular stress tensor working on the fluid element	[N/m^2]
α	Area fraction	-
ΔG	Gibbs free energy	[J]
ΔG_s	Surface excess free energy	[J]
ΔG_v	Volume excess free energy	[J]
Δg_v	Energy released due to solid formation per volume	[J]
ΔG_{crit}	Critical Gibbs free energy	[J]
ΔM_{dis}	Maximum displacement	[m]
ΔP	Pressure drop	[m]
ΔP_{dis}	Preloaded displacement	[m]
ΔT	Subcooling	[K]
δ	Overlap distance without changing the shapes	[m]
η	Damping coefficient of the dash-pot	-
γ	Shear rate	[s^{-1}]
ω	Angular velocity vector	[rad/s]
μ	Dynamic viscosity	[Pa s]
ν	Poisson ratio	-
Φ	Intermolecular potential energy	[J]
ϕ	Volume fraction	-
Φ_{net}	Lennard-Jones potential energy	[J]
Φ_{net}	Net potential energy of interaction	[J]
Φ_{rep}	Potential energy of repulsive interaction	[J]
ϕ_{tran}	Transition volume fraction	-
Φ_{vdw}	Potential energy of attractive interaction	[J]
ϕ_w	Volume fraction of the water phase	[-]
ψ	Modification constant	-

ρ	Density	[kg/m^3]
ρ_w	Wall material density	[kg/m^3]
σ	Surface energy	[N/m]
σ_c	Capillary force	[N/m]
τ_w	Wall shear	[N/m^2]
θ	Contact angle	[°]
ε	Depth of the potential well	[J]
r_0	Separation distance when $\Phi = 0$	[m]

Latin letters

$\dot{p}$	Particle flow rate	[s−1]
$\mathbf{n}$	Normal unit vector	-
$\overline{u}$	Average fluid velocity	[m/s]
A	Cross section area	[m^2]
a_b	Bridge curvature radius	[m]
A_H	Hamaker constant	[J]
a_l	Liquid bridge radius	[m]
A_p	Pipe cross section area	[m^2]
b	Roughness	[m]
B_{rep}	Van der Waals repulsive interactions	[kcal/mol]
B_{vdw}	Van der Waals attractive interactions	[kcal/mol]
C	Inter particle spacing	[m]
D	Particle diameter	[m]
E	Young‘s modulus	[Pa]
F	Force	[N]
f	Friction coefficient	-
$F(r)$	Intermolecular net force between two molecules with separation distance like r	[N]
f_b	Multiplication model blending factor	-
F_g	Gravitation force	[N]
F_{adh}	Adhesion force	[N]
F_{coh}	Cohesion force	[N]
F_{co}	Contact force	[N]
$f_{d,\Sigma}$	Specific inter-phase momentum transfer term	[N/m^3]
F_{dr}	Drag force	[N]
F_{liq}	Liquid bridge force	[N]
F_{lr}	Spin force	[N]
F_{ls}	Shear force	[N]

F_l	Lift force	[N]
G	Relative particle velocity	[m/s]
G_{ct}	Relative particle velocity at contact point	[m/s]
H_p	Height of the pipe	[m]
J	Impulsive force	[N · s]
k	Spring constant/stiffness of the spring	[N/m]
L_p	Length of the pipe	[m]
m	Mass	[kg]
n	Number of dispersed particles	-
p	Pressure	[Pa]
Q	Volume flux	[m^3/s]
R	Particle radius	[m]
r	Separation distance between two molecules	[m]
r_0	Separation distance between two molecules for $\Phi = 0$	[m]
R_{crit}	Critical cluster size	[m]
R_{min}	Minimum radius of surfaces in contact	[m]
T	Temperature	[K]
u	Continuous fluid velocity	[m/s]
u_{gas}	Gas velocity	[m/s]
u_{in}	Velocity inlet	[m/s]
u_{mix}	Mixture velocity	[m/s]
v	Dispersed particle velocity	[m/s]
v_{wall}	Top wall velocity	[m/s]
W_{adh}	Work of adhesion	[J/m^2]
W_{coh}	Work of cohesion	[J/m^2]
z	Separation distance between two particles	[m]

Subscripts

1	Material 1
2	Material 2
c	Continuous phase
d	Dispersed phase
i	Particle i
j	Particle j
n	Normal
pp	Plate-plate
sp	Sphere-plate
ss	Sphere-sphere
t	Tangential

Contents

Acknowledgements i
Abstract ii
Nomenclature iii
List of Figures xii
List of Tables xiv

1 Introduction **1**
1.1 Background and Motivation 1
1.2 Objective 2

2 Theory **3**
2.1 Gas Hydrates 3
2.1.1 Hydrate Structures and Stability Condition 3
2.1.2 Hydrate Kinetics 5
2.1.3 Gas Hydrate Plugging Scenarios 7
2.1.4 Hydrate Prevention in Industries 9
2.2 Adhesion and Cohesion Force 10
2.2.1 Van der Waals Forces 11
2.2.2 Liquid Bridge Forces 14
2.3 Computational Fluid Dynamic (CFD) 14
2.3.1 The Governing Equations of CFD 15
2.3.2 Discretization and Mesh 17
2.3.3 Physical Boundary and Initial Conditions 17
2.4 Modelling Multiphase Systems 18
2.4.1 Phase Coupling 18
2.4.2 Turbulence 19
2.4.3 Eulerian-Lagrangian vs. Eulerian-Eulerian 19
2.4.4 Modelling Particle Collision 20
2.4.5 Modelling the Dispersed Phase 23

3 Literature Survey **27**
3.1 Experimental Investigation of Hydrate Adhesive and Cohesive Forces 27
3.2 Experimental Investigation of Agglomeration and Deposition . . 31
3.3 Numerical Investigation of Agglomeration and Deposition 33

4 Methodology **37**
4.1 Methodology for Simulation of Hydrate Adhesive/Cohesive Forces 37
4.1.1 Geometry and Mesh . . . 37
4.1.2 System Description . . . 37
4.1.3 Models and Solvers . . . 38
4.1.4 Particle Injector . . . 39
4.1.5 Process Parameters . . . 39
4.1.6 Simulation Procedure and Calculations . . . 40
4.2 Methodology for Simulations of Hydrate Agglomeration and Deposition . . . 41
4.2.1 Geometry and Mesh . . . 41
4.2.2 System Description . . . 42
4.2.3 Models and Solvers . . . 43
4.2.4 Particle Injector . . . 45
4.2.5 Process Parameters . . . 46
4.2.6 Simulation Procedure . . . 47
4.2.7 Post Processing Tools . . . 47

5 Results and Discussion **49**
5.1 Hydrate Contact Forces . . . 49
5.2 Work of Cohesion/Adhesion . . . 51
5.3 Hydrate Agglomeration and Deposition . . . 53
5.3.1 Hydrate Agglomeration . . . 54
5.3.2 Hydrate Deposition . . . 62
5.4 Comparison with Other Works . . . 64

6 Conclusion **67**

7 Future Work **69**

Appendices **71**

A Material Properties **73**

B Conversion of Forces **77**

C Fortran Code **81**

D Importance of Cell Size in the Fortran Code **85**

Bibliography **87**

List of Figures

2.1 Methane hydrate cage. 3
2.2 Hydrate cavities and structures. 4
2.3 P-T diagram representing hydrate equilibrium conditions. 5
2.4 Gibbs free energy as a function of cluster size. 6
2.5 Gas consumption as function of time for hydrate formation. . . . 7
2.6 Gas hydrate formation and plugging mechanism in a oil dominant system. 8
2.7 Gas hydrate formation and plugging mechanism in a gas dominant system. 8
2.8 Gas hydrate formation and plugging mechanism in a system with high water cut. 9
2.9 Lennard-Jones potential function 12
2.10 Illustration of three of the most common macroscopic systems for the use of Hamaker theory. 12
2.11 Liquid bridge between two spheres. 14
2.12 Three main approachhes for numerical simulation of particles. . . 20
2.13 Soft sphere model contact force. 21
2.14 Illustration of pressure and shear force acting on an element. . . 24
2.15 Particle shear lift force. 24
2.16 Particle spin lift force on a rotating particle. 25

3.1 Illustration of hydrate debounding and tensile failure. 27
3.2 Illustration of hydrate shear force measurment. 28
3.3 Illustration of the shearing element cutting through the hydrate layer. 29
3.4 Procedure of MMF adhesion force measurement. 29
3.5 Procedure of MMF cohesion force measurement. 30
3.6 Schematic of the flowloop used by Josh et al. 31
3.7 Model of hydrate plug formation mechanism in 100 vol.% water cut systems. 31
3.8 Film growth mechanism in water dominated systems. 32
3.9 Schematic illustration of ice-water slurry flow. 33

4.1 Illustration of the spherical particle simulated. 38
4.2 Illustration of the cohesive/adhesive particle simulated in STAR CCM+. 40
4.3 Illustration of the experimental flow system. 41

4.4 Illustration of the simulated flow system. 42
4.5 Illustration of fluid velocity fields for case 1 and case 2. 43
4.6 Force balance on a particle in contact with a wall 44
4.7 Illustration of the two types of injectors used, random and surface injector. 45

5.1 Adhesion and cohesion hydrate force plotted against subcooling. 49
5.2 Work of adhesion and cohesion of hydrates. 52
5.3 Fluid velocity profiles for case 1 and 2 without particles. 53
5.4 Maximum particle connected component size as a function of time. 54
5.5 The maximum number of connected particles when the one-way coupling was selected in the model for case 1. 55
5.6 Maximum particle connected component size when the two-way coupling was selected in the model for case 1. 56
5.7 Particle connected component size and the average particle connected component size as a function of the vertical y-direction of the pipe for case 1. 56
5.8 The relative volume fraction and area fraction of hydrate particles as a function the the vertical y-direction of the pipe for case 1. . 57
5.9 Maximum particle connected component size when the one-way coupling was selected in the model for case 2. 58
5.10 Maximum particle connected component size when the two-way coupling was selected in the model for case 2. 59
5.11 Particle connected component size and the average particle connected component size as a function of the vertical y-direction of the pipe for case 2. 59
5.12 The relative volume fraction and area fraction of hydrate particles as function of the vertical y-direction for case 2. 60
5.13 Illustration of flocculation in agglomeration size for case 1. 61
5.14 Illustration of flocculation in agglomeration size for case 2. 61
5.15 Particle velocity near the top and the bottom wall for case 1. . . 62
5.16 Minimum and maximum particle velocity as a function of time for case 1. 63
5.17 Particle velocity near the top and the bottom wall for case 2. . . 63
5.18 Minimum and maximum particle velocity as a function of time for case 2. 64
5.19 Work cohesion for real and model hydrates. 64

D.1 Comparison of area fraction calculated based on different cell sizes for case 1. 85
D.2 Comparison of area fraction calculated based on different cell sizes for case 2. 86

List of Tables

4.1 Physical models and solvers in STAR CCM+ used for this simulations. 38
4.2 Process parameters. 39
4.3 Physical models and solvers in STAR CCM+ used for this simulations. 43
4.4 Process parameters. 46

5.1 CH_4-CS adhesion force from Klyusov et al. 52
5.2 CH_4/C_2H_6 hydrate cohesion force from Wang et al. 52
5.3 CH_4/C_2H_6 hydrate cohesion force from Lee et al. 53

A.1 Wall material properties. 73
A.2 Table of surface energy values of solid materials. 74
A.3 Tabel of hydrate density. 74
A.4 Static friction coefficient between ice and different wall materials. 75

B.1 CH_4/C_2H_6 hydrate cohesion force from Lee et al. 77
B.2 CH_4/C_2H_6 hydrate cohesion force and adhesion force to CS surface from Wang et al. 77
B.3 Hydrate anhesion/cohesion force from Jung et al. 78
B.4 CH_4 hydrate-CS adhesion force from Klyus ov et al. 78
B.5 CyC5 hydrate-CyC5 hydrate cohesion force and CyC_5 hydrate-CS adhesion force from Nicolas et al. 78
B.6 Hydrate adhesion fore to carbon steel from Groisman et al. . . . 79
B.7 Hydrate adhesion fore to duralumin from Groisman et al. 79
B.8 Hydrate adhesion fore to fluoroplastic from Groisman et al. . . . 80

Chapter 1

Introduction

This chapter briefly gives the background, motivation and objectives for this thesis.

1.1 Background and Motivation

Natural gas hydrates are solid crystalline compounds that form when water and natural gas combine at low temperature and high pressure. They represent a huge energy source, but also constitute a well known challenge in the oil and gas industry. In 1934, Hammerschmidt discovered for the first time that hydrates were capable of plugging petroleum pipelines [1]. Flowlines for oil and gas transport typically operate at low temperature and high pressure conditions, which are well within the hydrate formation stability region.

Cohesive particles like gas hydrates tend to adhere to each other and form larger particles, which macroscopically may be referred to as agglomerates. They also tend to adhere to surface material with different material properties, like pipeline walls. This process of gas hydrate adhesion to wall is based on the same mechanism as agglomeration and is referred to as deposition. In conventional transportation of oil and gas in multiphase flowlines, water will typically be present. Then gas hydrate particles can form, agglomerate, deposit and accumulate in the flowlines, consequently leading to plugging which can result in production stop until they are removed. In the worst case scenario they can constitute a safety concerns due to potential pressure build-up in the flowlines and a substantial economic risk [2].

Formation of gas hydrates in systems with high water content is one of the major challenges in the petroleum industry today. Conventional methods for hydrate prevention focus on the use of chemical inhibitors to shift the equilibrium curve for hydrate formation to higher pressure and lower temperatures (thermodynamic inhibitors). This methods are costly, energy intensive and environmentally unfriendly [3] due to the large water volumes. Therefore alternative methods for

hydrate prevention are of great interest. Nowadays, the modern strategy for hydrate mitigation focuses on risk management perspective of controlling hydrate formation instead of total prevention. Hydrates are allowed to form as long as the hydrate formation does not lead to plugging ("anti-agglomerates" and kinetic inhibitors), but this strategy has not yet been adopted due to insufficiently understanding of the water-hydrate slurry dynamics [4, 5].

It is crucial to develop a comprehensive understanding of hydrate blockage mechanisms, including deposition and agglomeration to find good solutions, which can prevent the problem in the future [6]. There are relatively few studies on hydrate agglomeration and deposition in water dominated systems. The hydrate adhesive and cohesive forces are responsible for these phenomena, and good estimates are important for obtaining accurate numerical simulations. Most force studies have considered cohesion forces between hydrate particles or ice particles, but few investigations have examined the adhesion force between particles and different surface materials [3].

1.2 Objective

The objective of this thesis was to run computational fluid dynamic simulations (CFD), using the simulation software STAR CCM+ with the purpose of numerically investigate the process of hydrate agglomeration and deposition in a high water cut system.

First, to achieve an accurate picture of the agglomeration and deposition process in the system, the contact forces were estimated from experiments, and the corresponding work of adhesion/cohesion for the investigated system was numerically measured. Afterwards, the mechanism of hydrate plugging in high water cut systems was numerically investigated by two models: one that allows for simulating the same material for as long as desired, and the other that allows for studying particles passing once through the simulated pipe length.

Chapter 2

Theory

This chapter provides an introduction to gas hydrates, as well as plugging scenarios and prevention methods. The different origins of particle cohesion and adhesion for hydrates are introduced in addition to some physical and mathematical models for particle-particle and particle-wall interaction. Furthermore, an introduction to computational fluid dynamics and its application, as well as an introduction to modelling of multiphase systems, are given.

2.1 Gas Hydrates

This section gives an introduction the to gas hydrate structure, stability, kinetics, plugging scenarios in the industry and known prevention methods.

2.1.1 Hydrate Structures and Stability Condition

Gas hydrates (also referred to shortly as hydrates) are crystalline water based ice like compounds. In contrast to hexagonal ice, gas hydrates contain small guest molecules, such as methane, ethane, propane and carbon dioxide encapsulate inside spatial cages of hydrogen bonded water molecules. Fig. 2.1 shows a schematic drawing of a methane hydrate cage structure.

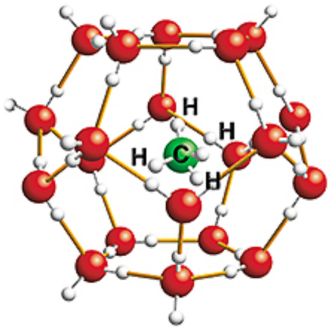

Figure 2.1: Methane hydrate cage from the webpage of Schlumberger [7].

The water molecules are referred to as host molecules, and the other compounds are called "guest" molecules or "formers." The guest molecule stabilizes the structure due to the formation of non chemical bonding called van der Waals force to the water lattice [8]. This force will appear when atoms, molecules, or combination of both gets close enough to influence each other. This issue is discussed in more detail in section 2.2.

The hydrate structure depends on the size of the guest molecules. Both hydrate structure I (SI) and II (SII) have a cubic crystal structure, while hydrate structure H (SH) is hexagonal [9]. Hydrate SI contains small guest molecules, 0.4-0.55 nm, as CH_4, CO_2 and C_2H_6, while hydrate SII occurs with larger guest molecules, 0.6-0.7 nm, such as C_3H_8 and C_4H_8 (isobutane). The hexagonal SH occurs only with a mixture of small and large, 0.8-0.9 nm guest molecules. Small molecules like CH_4 stabilize the small and medium cages, and large guest such as C_7H_{14} stabilizes the large cages [10, 11]. SI consists of 46 water molecules, 2 small 5^{12} and 6 large $5^{12}6^2$ cavities, SII consists of 136 water molecules, 16 small 5^{12} and 8 large $5^{12}6^4$ cavities and structure H consists of 34 water molecules, 3 small 5^{12}, 1 large $5^{12}6^8$ and 2 medium$4^3 5^6 6^3$ sized cavities [11] as illustrated in Fig. 2.2. All the structures need to fill its cavities to prevent hydrogen-bond strain and breakage. They contain all both large and small cavities, and sometimes the large guests are too large for the small cages, so that they have to remain empty. Small molecules can, in contrast, fill both cages.

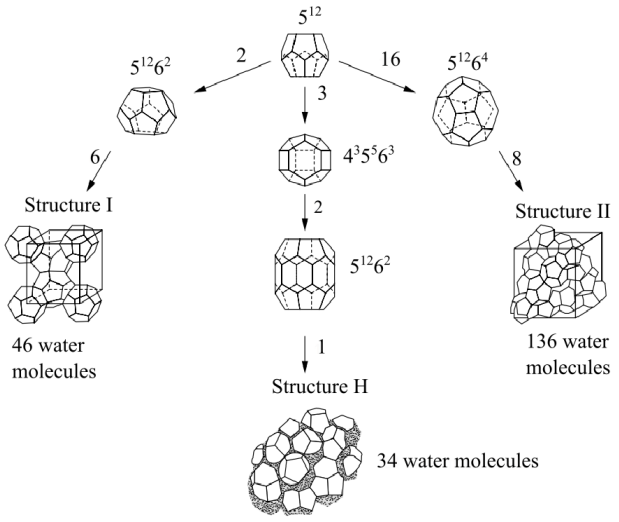

Figure 2.2: An overview of different cavity types that combine to form hydrate structure I, II and H (sI, sII and sH) [12].

Natural gas hydrates are not stable under normal conditions, and this is related to the fact that the system needs to be energetically intensive to be able to incorporate the gas molecule into the water structure [13]. The favourable condition for hydrate formation is a high pressure and a low temperature. Hydrates can form at temperatures above 0°C as long as the pressure is high enough. The

exact temperature and pressure depend on the composition of guest molecules. The stability region for hydrates is given by a P-T diagram, where the hydrates stability region occurs above the equilibrium curve in Fig. 2.3.

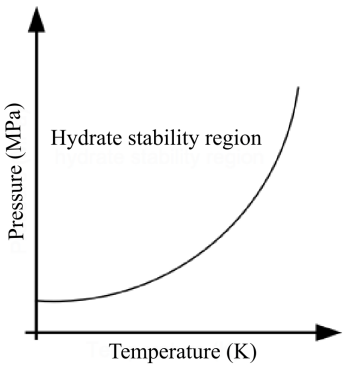

Figure 2.3: Example of a P-T diagram representing hydrate equilibrium conditions [13].

If either the pressure, p or the temperature, T is known, the other parameter can be predicted for the most common simple natural gas components by the known P-T diagram or the following equation:

$$p[\text{kPa}] = e^{(a+\frac{b}{T[\text{K}]})}, \tag{2.1}$$

with table values for a and b found in [10]. In the case of multi-component hydrate formers, it is possible to find a similar dependence. The "gas gravity method" is the easiest approach for determining equilibrium conditions for mixture hydrates. Sloan [10] describes this method and other more precise correlations in more detail.

2.1.2 Hydrate Kinetics

Hydrate formation in a liquid-gas system starts with nucleation. In this process, small clusters of water and gas grow and break down in an attempt to achieve a critical size for stable growth [14]. Before the clusters reach the critical size they are unstable, meaning that an increase in the surface of the hydrate particle results in an rise in the Gibbs free energy of the solid phase, $\Delta G>0$. When the clusters reach the critical size, R_{crit}, an increase in the hydrate particle surface will reduce the Gibbs free energy of the solid phase, $\Delta G<0$ [13], as shown in Fig. 2.4.

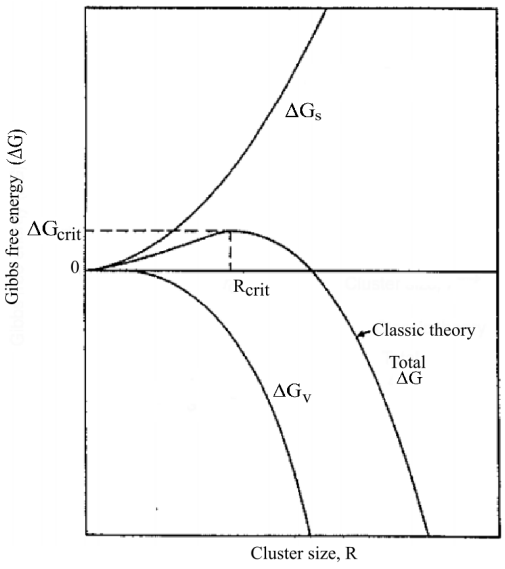

Figure 2.4: Gibbs free energy as a function of cluster size adapted from Salon [14].

An equation describing the Gibbs free energy of the solid phase relative to that of a homogeneous solution in case of spherical particles can be expressed as [14]:

$$\Delta G = \Delta G_s + \Delta G_v = 4\pi R^2 \sigma + \frac{4}{3}\pi R^3 \Delta g_v \leq 0. \tag{2.2}$$

The parameter Δg_{v} is the free energy change per unit volume, R is the hydrate nuclei radius, and σ is the energy gain for the formation of new surface per unit surface [14, 13]. The total Gibbs free energy change due to the growing of hydrate cores is then a competition between two contributions of opposite sign. The positive contribution is the surface excess free energy ΔG_{s}, which is the work needed to push away the environmental phase, and provide space for hydrates. This is an energy demanding process and it is the dominating term in Eq. (2.2) before the hydrate reaches the critical size. The negative contribution is the volume excess free energy ΔG_{v}, which is the energetic advantage of forming the hydrates. This term has to be negative for the phase transition to occur and is the dominating term in Eq. (2.2) after reaching the critical size.

The homogeneous nucleation scenario described above represents an idealized case of nucleation, which takes place in a supersaturated system. No impurities are present here, in contrast to the case of heterogeneous nucleation where impurities are present and act as nucleation centers or nucleation sites. With the presence of impurities like microparticles, liquid droplets or gas bubbles, the energy gain for hydrate formation reduces and the formation of hydrate nuclei is more likely to occur.

After the nucleation period, stable hydrate crystals have been formed. Then the induction time starts, which is the time for onset of massive growth. At this stage, hydrate can be detected macroscopically [15]. This time period depends on the level of supersaturation and the amount of impurities present. Massive growth takes place through the further incorporation of gas molecules into the water cages. The gas hydrate growth rate depends on the rate of gas diffusion through the liquid to the particle surface, which in turn depends on the particle size as well as turbulence intensity and physical properties of the carrier fluid [13]. Fig. 2.5 shows the gas consumption as a function of time. It can be seen from the figure that when the cavities become more and more filled, less gas is consumed, and the cavities begin to fill up.

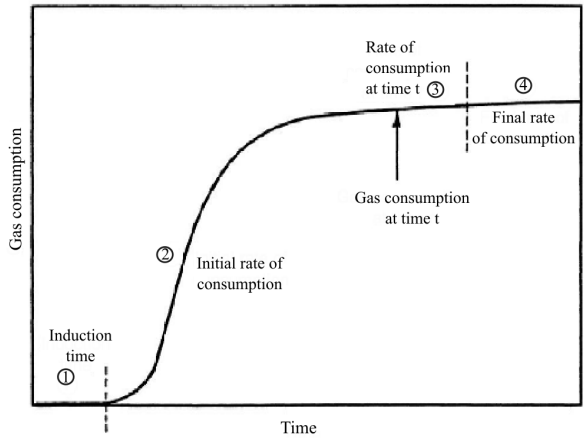

Figure 2.5: Gas consumption as function of time for hydrate formation. The figure is adapted from Sloan [14].

2.1.3 Gas Hydrate Plugging Scenarios

The scenario of gas hydrate formation and plugging is system dependent. Petroleum systems can either be oil dominated, gas dominated or water dominated. The process of nucleation is different for these systems, leading to different scenarios for plugging. Hydrate formation and plugging mechanism are best known for oil dominated, but less understood for gas dominated systems, and even less understood for water dominated systems. As subsea petroleum fields mature, the amount of water produced increases, which results in an increased risk of gas hydrate plug formation in the flowlines [5]. The production stream during the life of a reservoir will eventually lead to a water-dominated system, with water as the hydrate carrier phase [16]. This thesis, therefore, makes an effort to better understand the behaviour of hydrates and fluid impact in high water cut systems.

In the case when pipelines are filled with mainly hydrocarbon liquid, hydrates tend to form on the surface of dispersed water droplets in the oil phase and form a solid shell around them. This shell will delay further conversion of the water core due to very slow diffusion of gas molecules through the shell.

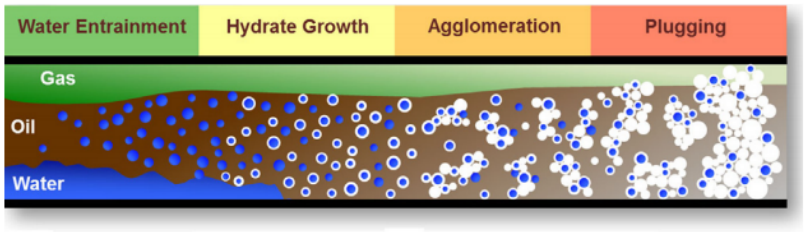

Figure 2.6: Gas hydrate formation in a oil dominant system with low water cut [5].

Fig. 2.6 shows the stages in the process of plugging in an oil-dominated system. Hydrates are formed in the bulk phase at the interphase between dispersed water droplets and the continuous oil phase. Cohesive forces between hydrate shell/particles result in formation of large agglomerates, increased viscosity and reduction in flow velocity, which enables localized particle build up and jamming type failure [17]. Hydrates and agglomerates may also stick to the pipeline wall due to particle-wall interaction leading to hydrate growth on the wall, a phenomenon called deposition. A model for hydrate growth and plugging in oil-dominated systems called the Colorado School of Mines Hydrate Kinetics has been developed [18, 16]. This model is incorporated into the dynamic oil and gas multiphase simulator OLGA. Due to the main assumption of all water beeing emulsified in the oil phase, the model is practically suited for water in oil systems, whereas its performance in flow systems with free water phase present is questionable [5, 4].

In the case of a gas dominate system, the process of nucleation is different. The water is present in vapour phase and will tend to condense on the pipeline wall of typically lower temperature than the equilibrium temperature for the gas-water vapour flow. As the hydrate layer grows, it will act as an insulating layer that will tend to slow down the further growth of the layer. In this case, we get hydrate formation on the pipeline walls, in contrast to the liquid dominant system where hydrates form in the bulk. The mechanism of plugging for a gas dominated system can be described by three stages illustrated in Fig. 2.7.

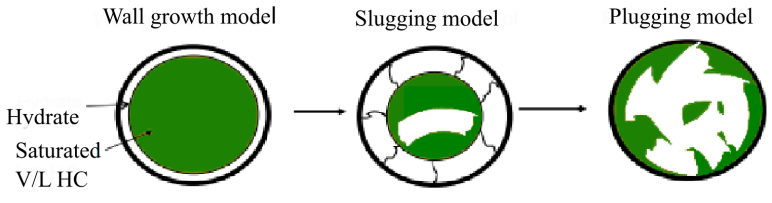

Figure 2.7: Gas hydrate formation and plugging mechanism in a gas dominant system adapted from Nicolas et al. [19].

The first stage is wall growth, which means that hydrates start to growth or built up on the pipeline wall. The second stage is slugging, which means that the hydrates on the wall reach a critical mass and collapse. The last stage is plugging, which means that removed hydrate aggregates are transported with the flow, that may lead to plugging further into the pipe. Another possible mechanism of hydrate plugging as result of hydrate growth on the wall could be build up of a hydrate layer that eventually blocks the pipeline flow.

During the later stages of a field life, the amount of produced water increase, resulting in a high water cut system with a free water phase present. As mentioned previously, the mechanisms of hydrate agglomeration and deposition leading to plugging in such high water content systems are poorly understood. It is hypothesized by Joshi et al. [5] that plugging in such systems occurs due to hydrate bed formation and wall deposition reducing the flow area.

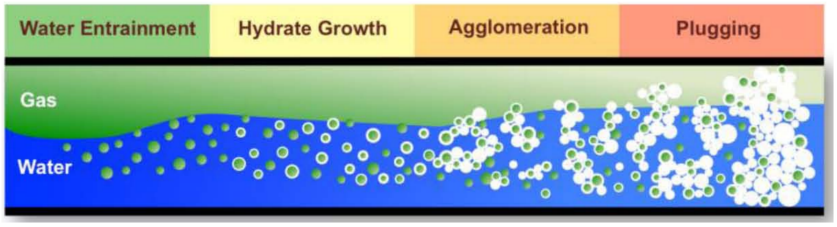

Figure 2.8: Gas hydrate formation in a system with high water cut [20].

In this thesis, the experimental system used by Joshi et al. are investigated numerically to give a more accurate picture of the mechanism of plugging. The previous work done for investigating gas hydrate agglomeration and deposition in water dominated systems is shown in section 3.2 and 3.3.

2.1.4 Hydrate Prevention in Industries

There are several techniques to avoid hydrate formation and plugging in pipelines. One option is to remove the free and dissolved water from the system by using an offshore dehydration plant or subsea separation, which is usually not the most cost effective solution for high water cut systems. Another option is to keep the temperature and pressure out of the hydrate stability region, or by adding additives called inhibitors.

Thermodynamic hydrate inhibitors (THIs) are the most conventional strategy employed to prevent hydrates. The presence of thermodynamic inhibitors (alcohols, glycerols or salts) causes a change in the P-T diagram. It reduces the size of the hydrate stability region by shifting the equilibrium curve in Fig. 2.3 to the left. The major effect of alcohols and glycerols are hydrogen bonding of water molecules, which is in direct competition with hydrate formation. Salt also tends to make water unavailable for hydrate formation, but in a different way. It ionizes in the solution and interacts with the dipoles of the water molecule with a very strong columbic bond. Water molecules are stronger attracted to

ions than to other water molecules, and to the hydrate formers. Salt is the most effective method, but it is not very much used in practice due to the strong corrosion effect of metal pipes; alcohols, in contrast, inhibit corrosion. A large concentration of THIs is needed for hydrate inhibition, especially in case of a large amount of water, which makes the technique to be expensive. The world-wide methanol (one of the most common used thermodynamic inhibitors) daily cost of hydrate inhibition are estimated to be US$740,000 [21]. To offset the high cost and amount of THI usage, low dosage hydrate inhibitors (LDHIs) have been developed (kinetic inhibitors and "anti agglomerates"), which allow for hydrate formation while they are minimizing the risk of plug formation.

Kinetic hydrate inhibitors (KHIs) do not prevent hydrate formation, but delay onset of massive hydrate growth. They are low concentration additives, which prevent hydrate growth by three mechanisms. The first one is the sterical mechanism, which causes H_2O reorganization into hydrate to become more difficult. The secound one is the "tipping in" mechanism, which means that some groups of the kinetic inhibitors may partially enter the hydrate cavity and block the further growth of hydrates. Finally, the third mechanism is the packing and transport delay mechanism, that creates thick films between the water and the hydrate former, which delays transportation between the two phases [22, 23]. These mechanisms for inhibition are limited at long times, low temperatures, and high pressure. Low-dosage KHIs are then not entirely suitable for high water content systems under high pressure and low temperature reservoir conditions investigated in this thesis.

The other type of LDIHs is "anti-agglomerates" (AAs), an interesting alternative to methanol. AAs adhere to the hydrate surface and cover the hydrate crystals by non-polar films that flow easily with liquid hydrocarbons. Hydrate crystals will then be able to flow together without adhering to larger agglomerates [15]. However, their efficiency drops in systems with high water cut. AAs have been found to be ineffective beyond a water cut of 50 vol.%. A significantly smaller amount of the LDHIs are needed than the THIs, but these methods are less understood. Development of new hydrate management strategies with low cost and zero plugging risk are limited by the understanding of the hydrate plug formation mechanism, which currently is limited to low water cut systems [5].

2.2 Adhesion and Cohesion Force

Adhesion forces are the attractive forces between different molecules, in contrast, cohesion forces are the attractive forces between similar molecules. Adhesive and cohesive forces may be due to different physical phenomena. Among those, most relevant for hydrate particle interactions are the van der Waals forces and the forces due to liquid bridge. In this thesis, only the van der Waals forces are considered. These forces are presented in detail, while just a brief introduction to the liquid bridge forces are given.

2.2.1 Van der Waals Forces

Van der Waals forces is a general term for forces acting between neutral molecules. They are distance dependent and will rapidly vanish at long distances between interacting molecules. The forces included in the term can be listed according to Berg [24]:

1. Interaction between permanently charged distributions, such as dipoles and quadrupoles.

2. Interaction that results when a molecule with permanent dipole induces a dipole in a neighboring molecule, called Debye force.

3. Two temporary induced dipoles caused by oscillations of the electron clouds of all molecules, called London dispersion force.

4. Repulsive forces which occur due to an overlap of electron clouds, this is called the Pauli exclusion principle.

The three attractive forces (1-3) are found to vary as a function of $1/r^6$, where r represents the molecules separation distance. This means that all the potential energy functions can be collected into one term:

$$\Phi_{vdw} = -\frac{B_{vdw}}{r^6}, \tag{2.3}$$

where Φ_{vdw} is the potential energy of interaction and B_{vdw} is a collective parameter for the different attractive interactions under the van der Waals term. This relationship holds only as long as the electron clouds of the interaction molecules do not overlap. Under such conditions, strong repulsive forces will arise, according to the Pauli exclusion principle. The exact functional form of the r-dependence of the repulsive interactions has not yet been fully established, but it can reasonably be represented by:

$$\Phi_{rep} = \frac{B_{rep}}{r^{12}}. \tag{2.4}$$

The total physical interaction between a pair of non-bonded and uncharged molecules is given by the sum of the van der Waals and repulsive interactions. The sum of Eqs. (2.3) and (2.4) yields the net van der Waals interaction energies:

$$\Phi_{net} = \frac{B_{rep}}{r^{12}} - \frac{B_{vdw}}{r^6}. \tag{2.5}$$

The Lennard-Jones potential is a simple mathematical model that approximates the interaction between a pair of neutral atoms or molecules given by the following equation:

$$\Phi_{L-J} = 4\varepsilon\left[\left(\frac{r_0}{r}\right)^{12} - \left(\frac{r_0}{r}\right)^{6}\right], \tag{2.6}$$

where r_0 is defined as the separation distance when the intermolecular potential between the particles is zero ($\Phi = 0$), and ε is defined as the depth of the "potential well", a measure of how strong the two particles attract each other.

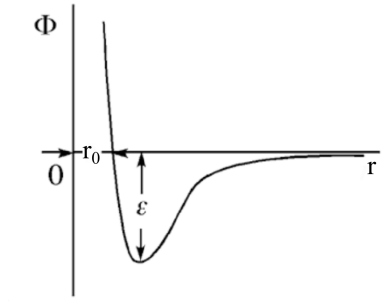

Figure 2.9: Schematic representation of the Lennard-Jones potential function adapted from Berg [24].

The derivative of the potential energy, Eqs. (2.5) and (2.6) with respect to r (the slope of the potential energy function shown in Fig. 2.9), yields the intermolecular net force between two molecules:

$$F(r) = \frac{d\Phi_{net}}{dr} = -\frac{24\varepsilon}{r}\left[2\left(\frac{r_0}{r}\right)^{12} - \left(\frac{r_0}{r}\right)^{6}\right]. \tag{2.7}$$

The van der Waals interaction force involves only two molecules. Hamaker proposed a theory which expanded these interactions to be solved on a macroscopic level, meaning that contribution from the many molecules constituting the surface was taken into consideration [25].

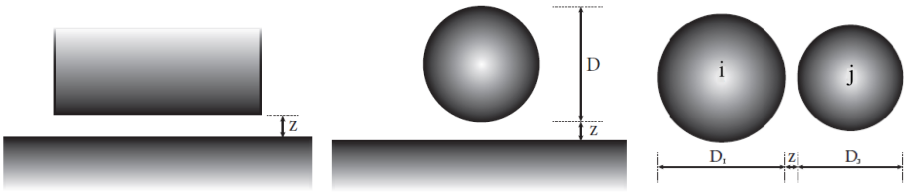

(a) Two flat plates **(b)** Sphere and plane **(c)** Two spheres

Figure 2.10: Illustration of three of the most common macroscopic systems for the use of Hamaker theory for solving the van der Waals interactions, adapted from Hellestø et al. [26]. The parameter z represents the distance between two objects and D represents the sphere diameter.

The Hamaker approach to calculate the interaction force between two microscopic bodies, makes use of the following formulas in the case of two flat plates, a sphere and a plate and two spheres respectively, as illustrated in Fig. 2.10:

$$F_{pp} = \frac{A_H}{6\pi z^3}, \tag{2.8a}$$

per area and

$$F_{sp} = \frac{A_H D}{12 z^2}, \tag{2.8b}$$

$$F_{ss} = \frac{A_H}{12 z^2} \frac{D_1 D_2}{D_1 + D_2}, \tag{2.8c}$$

where A_H is referred to as the Hamaker constant, D is the sphere diameter and z is the separation distance between two objects, valid for $D \gg z$. The separation distance can in this case be taken to 0.38 nm, which is the mean free path of methane molecules [27]. It has also been suggested to modify these equations by replacing z with $z + b$, where $b = (b_1 + b_2)/2$ and b_1 and b_2 are the roughness of the surfaces. In this thesis, the roughness of hydrate was set to 0.744 nm, which is the size of a methane hydrate nuclei [28].

The Hamaker constant between different materials in a system is given by:

$$(A_H)_{12} = \sqrt{(A_H)_{11} \cdot (A_H)_{22}} \tag{2.9}$$

for a dry system, where $(A_H)_{11}$ and $(A_H)_{22}$ are the Hamaker constants for each material.

Work of cohesion, W_{coh}, is in accordance to Israelachvili [29], defined as the work per unit area needed to separate two cohesive rigid planar surfaces of the same material in a vacuum, which is therefore equal to twice the surface energy, σ, and the equation is given as:

$$W_{coh} = 2\sigma. \tag{2.10}$$

The surface energy of a solid reflects the nature of the bonds, either strong or weak, between atoms. For strong bonds, typical values range between 100 and 500 mJ/m^2 for ionic crystals to 1000–3000 mJ/m^2 for most metals [30]. Surface energy values for different materials are shown in appendix A.

For two different surfaces, 1 and 2, with non-zero interface energy, the work of adhesion can be expressed as:

$$W_{adh} = \sigma_1 + \sigma_2 - \sigma_{12}, \tag{2.11}$$

where σ_{12} is the interfacial energy per unit area, given by the following equation:

$$\sigma_{12} = \sigma_1 + \sigma_2 - 2\sqrt{\sigma_1 \sigma_2} = (\sqrt{\sigma_1} - \sqrt{\sigma_2})^2. \tag{2.12}$$

2.2.2 Liquid Bridge Forces

The phenomena of liquid bridge become crucial in wet systems or systems with high humidity causing liquid to condense on surfaces [25]. In the case of two or more solid bodies in contact with the same liquid, such that they "share" meniscus, capillary forces act between the solid bodies, tending to either draw them together or push them away from each other. The liquid between the two particles tends to be drawn towards the particle contact point due to surface tension. The surface tension also causes the liquid interface between the two contacting particles to be concave, which leads to a low/negative pressure within the bridge. This pressure difference and the capillary force constitute the cohesive force from the liquid bridging. The final relation for cohesive force between two particles due to liquid bridge is:

$$F_{liq} = \pi a_l^2 \sigma_c \left(\frac{1}{a_b} + \frac{1}{a_l} \right) + 2\pi a_l \sigma_c cos\theta, \tag{2.13}$$

where σ_c is the capillary force, a_b is the bridge curvature radius, a_l is the liquid bridge radius, as illustrated in Fig. 2.11 and θ is the contact angle between the liquid and particle surface [25].

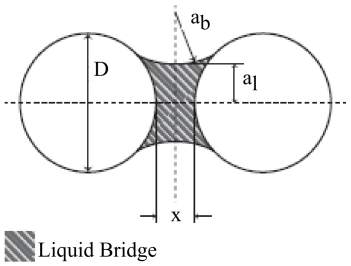

Figure 2.11: Illustration of liquid bridge between two spheres [25]. D is the sphere diameter, x is the separation distance, a_b is the bridge curvature radius and a_l is the liquid bridge radius.

2.3 Computational Fluid Dynamic (CFD)

CFD is the simulation of fluid flow systems using modelling (mathematical and physical problem formulation) and numerical methods (discretization methods, solvers, process parameters, grid generation, etc.). Numerical simulations are an alternative to physical experiments and can be very valuable in situations where experiments can be difficult to carry out in practice. The CFD software used in this thesis was the STAR-CCM+ version 12.02.010 from Siemens. This software provides its user by the ability to model complex geometries, in turn, generate a mesh, make use of models for taking into account different physical phenomena. Simulations can be performed by running cores in parallel and post-processing tools are available in the program.

2.3.1 The Governing Equations of CFD

CFD is based on three fundamental governing equations of fluid dynamics: the continuity, momentum and energy equations. They are the mathematical statements of three fundamental physical principles upon which all of fluid dynamics is based [31]:

1. Mass is conserved
2. Newton‘s second law (Force = Mass x Acceleration)
3. Energy is conserved

To investigate a fluid flow, we have to know the physical properties of the flow and use mathematical formulations to describe the physical properties. The governing equations can be derived in four different forms depending on the model of the flow. They can be expressed as partial differential equations or as integral equations. The partial differential equations are derived from an infinitesimally small fluid element, whereas the integral equations are derived from a finite control volume. In both cases, the fluid element can be either fixed in space or moving with the flow. The element fixed in space will give equations in the conservation form, while the element moving with the fluid will result in the non-conservation form of these equations.

When describing a viscous flow, these fundamental flow equations are called Navier-Stokes Equation. A viscous flow means a flow where the transport phenomena of friction, thermal conductivity, and/or mass diffusion are included, and they will always contribute to increasing the entropy of the flow. In contrast, if the flow is non-viscous the equations are called Euler equation, and in this case, the dissipative transport phenomena of viscosity, mass diffusion, and thermal conductivity are neglected. This task deals with a viscous flow and then the numerical solution of the Navier-Stoke equation.

Continuity Equation

The governing flow equation, which is obtained by application of the physical principle of mass conservation to any one of the four flow models described above is called the continuity equation, which states that:

Rate of mass accumulation inside fluid element
=
Rate of mass flow in to element - Rate of mass flow out of element

The form of the equations, which is most relevant for the continuous fluid in this thesis, is the partial differential equation in conservation form. The continuity equation can be presented as follows:

$$\frac{\partial}{\partial t}(\phi_c \rho_c) + \nabla \cdot (\phi_c \rho_c \mathbf{u}) = 0, \tag{2.14}$$

where ϕ_c is the volume fraction of the contineous phase, ρ_c is the density of the continuous phase and $\mathbf{u}$ is the fluid velocity vector [32].

Momentum Equation

The governing flow equation, which results from the application of the physical principle of Newton's second law is the momentum equation. When applying the Newton's second law to a moving fluid element, it tells us that net force on the fluid element equals its mass times the acceleration of the element. There are two different sources of forces acting on the moving fluid element:

1. *Body forces*: these forces act directly on the volumetric mass of the fluid element at a distance from it. Examples are gravitational, electric, and magnetic forces.

2. *Surface forces*: these forces act directly on the surface of the fluid element. The outside fluid imposes two sources of surface force, pressure and viscous forces. The pressure force involves the total pressure acting on the element surface by the surrounding fluid. The viscous forces include the shear and normal stress distribution acting on the surface, imposed by the outside fluid by means of friction.

The momentum equation in the conservative differential form can be expressed as:

$$\frac{\partial}{\partial t}(\phi_c \rho_c \mathbf{u}) + \nabla(\phi_c \rho_c \mathbf{u}\mathbf{u}) = -\phi_c \nabla p + \nabla \cdot (\phi_c(\boldsymbol{\tau} + \boldsymbol{\tau}^{\boldsymbol{t}})) - \mathbf{f}_{\mathbf{d},\boldsymbol{\Sigma}}, \tag{2.15}$$

where p is pressure, $\boldsymbol{\tau}$ is the molecular stress tensor and $\boldsymbol{\tau}^{\boldsymbol{t}}$ tangential stress tensor working on the fluid element and $\mathbf{f}_{\mathbf{d},\boldsymbol{\Sigma}}$ denotes the specific inter-phase momentum transfer, resulting from drag and lift forces acting on particles (see section 2.4.5) [32, 33].

Energy Equation

The energy equation is based on the physical principle of energy conservation, which also is the first law of thermodynamics. The physical principle states that the total energy of an isolated system is constant. Energy can be transformed from one form to another, but can not be created or destroyed. When applying this physical principle to any one of the flow models, it states that:

Rate of change of energy inside fluid element
$=$
Net flux of heat into element
$+$
Rate of work done on element due to body and surface forces

In this thesis, the energy equation was not used in the model.

2.3.2 Discretization and Mesh

Discretization is the process of transforming the continuous closed-form equations described in section 2.3.1, into discrete algebraic equations, suitable for numerical computing. The closed form expression gives the variation of the dependent variable continuously through the domain, while the numerical solution can only give answers at discrete points in the domain, called grid points. Depending on the mathematical model, STAR-CCM+ discretizes the continuous equations using either the finite volume or the finite element method [32].

The procedure of discretization is first to divide the continuous domain into a finite number of subdomains (collection of elements or cells all together making up the mesh), next is to store the unknowns at specific locations of the mesh, like vertices, cell centroids, face centroids, or edges. Finally, the integral or differential equations are employed for discretization in space and time. The result is a coupled system of algebraic equations that need to be solved at each timestep [33]. The mesh can be generated in different ways resulting in subdomains of different shape and size. The type of mesh chosen for a given flow problem can determine the accuracy of the numerical solution obtained.

There are two different CFD techniques for solving the resulting algebraic equations, the explicit approaches, and the implicit approaches. For the explicit approach, each equation to be solved contains only one unknown and can therefore be solved in a straightforward manner. In contrast, for the implicit approach, used in this thesis, each equation to be solved contains more than one unknown, and the equations need to be solved simultaneously. The advantage of using the implicit approach is that stability can be maintained over a much larger time step, ΔT, than the explicit approach, resulting in a shorter computational time.

2.3.3 Physical Boundary and Initial Conditions

Flow fields can be quite different from each other, even if the governing equations are the same. The difference appears in the boundary conditions, which direct the motion of the flow. The boundary conditions, and sometimes the initial conditions, dictate the particular solution to be obtained from the governing equations. It is important to apply certain physical boundary conditions on the particular geometric surface for the numerical solutions to be accurate.

The most common boundary that comes upon in confined fluid flow problems is the wall. Usually, one has a set of impermeable walls, either stationary or moving that confine the flow and some walls that act as in- and out flow of the medium. The boundary condition for a viscous flow on a surface assumes no relative velocity between the wall surface and the fluid in immediate contact with the surface. This is known as non-slip boundary condition. A wide range of boundary condition types permits the flow to enter and exit the solution domain, inlet and outlet boundary that are surface through which fluid enters and leave the computational domain. The most common are velocity inlet and pressure

outlet. Boundary conditions can also be useful for saving computational time. Symmetry boundaries allow one to take benefit of physical flow symmetry, to reduce the size of the computation domain and periodic boundaries allow for the account of periodically repeating nature of the flow in the simulation and thus save memory and time.

The initial conditions are the values of the flow field variables at time $t = 0$, and the physical parameters to account for are typically velocity components, pressure, and temperature. These values should be set as close as possible to the expected steady-state solution. For steady-state computations, the initial conditions should not influence the converged solution, but setting the initial conditions to non-physical values or far away from the final solution values can affect the path to convergence and effort that is required to reach convergence.

2.4 Modelling Multiphase Systems

In all cases of multiphase flow, the system consists of a continuous phase and one or more dispersed phases mixed at a macroscopic level. A phase is defined by the thermodynamically different states of matter, such as solid, liquid and gas. This thesis considers only one dispersed phase represented by solid hydrate particles in either gas- or liquid continuous phase. The flow characteristic follows a dispersed phase flow, and for this reason, the governing flow equations need to be modified. Therefore, we need to introduce phase coupling, exchange of properties like momentum heat and mass, between the different phases.

2.4.1 Phase Coupling

Interactions between the dispersed and the continuous phase can be simulated as either one-way coupled or two-way coupled. With the one-way coupling, only the continuous phase influences the dispersed phase, and there is no influence in the opposite direction. In the case of the two-way coupling, the effect of the dispersed phase on the continuous phase is taken into account. In this thesis, both one-way and two-way coupling are considered and compared. In general, the dispersed phase is driven by the motion of the continuous phase. The continuous phase is affected by the dispersed phase and can exchange momentum, heat, and mass with the continuous phase. The interaction strength between the two phases depends on parameters like the size, density, and the number of dispersed particles.

2.4.2 Turbulence

Turbulent flow occurs in the case of a high Reynolds number, and is characterized by continuous instability and chaotic changes in pressure and flow velocity. This is in contrast to the laminar flow regime, which occurs in the case of a low Reynolds number, characterized by fluid flowing in parallel layers. It is possible to simulate turbulent flow directly by solving the Navier Stokes equations, but in practice the computer resources that are required are too large due to small scale and high frequency of fluctuations. Therefore, instead of solving the exact equations of turbulent flow, STAR CCM+ solves for averaged quantities by the Reynold-averaged Navier-Stokes (RANS) equations, and then approximate the impact of the small fluctuating structures. The most common RANS turbulence model used in STAR CCM+ is the two-equation k-ε model, which solves the transport equations for the turbulent kinetic energy and its dissipation rate to determine the turbulent viscosity. This is necessary to model the turbulent stress tensor, $\boldsymbol{\tau^t}$, which appears in the momentum transport equation (Eq. (2.15)) in the averaging process.

The effect of turbulence in phase distribution of the phase concentration is modelled by the turbulent dispersion model. This model collaborates with the RANS turbulent model in the physics continuum. A particle in a turbulent flow experiences a randomly-varying velocity field to which it responds according to its inertia.

2.4.3 Eulerian-Lagrangian vs. Eulerian-Eulerian

There are two main modelling approaches when modelling multiphase systems, the Eulerian-Lagrangian (E-L) and the Eulerian-Eulerian (E-E). The main difference between these approaches is how they consider the dispersed phase. The continuous phase is in both cases treated with the Eulerian approach, which means that the model solves the Navier-Stoke equation for the viscous fluid flow and the governing equation are modified to take into account the presence of the dispersed phase. In numerical simulations, the dispersed phase can be treated either in the Lagrangian or the Eulerian frame of reference. The E-L model track particles individual as they move through the continuous phase, and then solves the equation of motion for each particle. This model is very accurate, but computational extensive for a large number of particles. The E-E model, in contrast, considers the dispersed phase to be a continuous phase, as well as the carrier phase. The Navier-Stokes equation can then be solved for each present phase.

The three main approaches for numerical simulation of particles are the discrete element method (DEM), discrete parcel method (DPM) and two-fluid model (T-F) illustrated in Fig. 2.12.

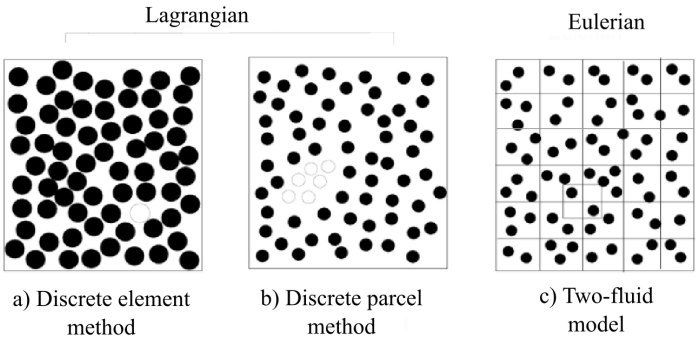

Figure 2.12: Three main approaches for numerical simulation of particles [25].

The two Lagrangian approaches DEM and DPM are represented in Figs. 2.12 a) and b) respectively. When using DEM, the motion of each particle is analyzed incorporating the fluid dynamic forces, the contact forces and the momentum due to the neighboring particles. This method requires relatively long computational time for a large number of particles. An alternative Lagrangian method requiring less computational time is the DPM, where parcels of particles are identified when moving through the field. Each particle in the parcel (open circles) are the same, so the parcel is represented by one computational particle. The third approach is the two-fluid (T-F) model, shown in Fig. 2.12 c). This model consider the dispersed solid phase as a continuous phase like the carrier fluid phase. This thesis aimed to study the behaviour of each particle and how they interact with each other and their surroundings. For this reason, the most accurate and suitable modelling approach for the dispersed phase in this thesis is the Lagrangian DEM approach.

2.4.4 Modelling Particle Collision

There are in general two different approaches when modelling DEM solid particle collisions, namely the soft-sphere and the hard-sphere models [34]. In this work, the DEM approach with the soft-sphere model was used. There exist several hard-sphere and soft-sphere collision models, where that presented by Crowe et al. [25] are among the most widely used and is shown in this thesis. The soft-sphere model and its derivation is described in detail while only a brief introduction to the hard-sphere model is given.

Soft Sphere Model

The soft-sphere model solves the differential equation of motion for the particles during the collision directly. This technique gives access to many details of each collision at the cost of being computationally demanding [35]. When solid bodies exert a force on each other, they deform. For a large number of particles, a certain simplification is inevitable in practical computation, and for

this reason, the soft sphere model was developed. The first simplification is that the influence of the particle of interest is limited to only neighbouring particles, which are in direct contact with the particle. Further, one assumes particles to overlap rather than deforming when they are in contact.

Two types of collisions are considered in this thesis: particle-particle, and particle-wall interactions. Fig. 2.13 shows the case of a particle-particle collision when a particle i interacts with a particle j obliquely. In the soft-sphere model, the two particles overlap with a distance δ_n in the normal direction and δ_t in tangential direction without changing their shape.

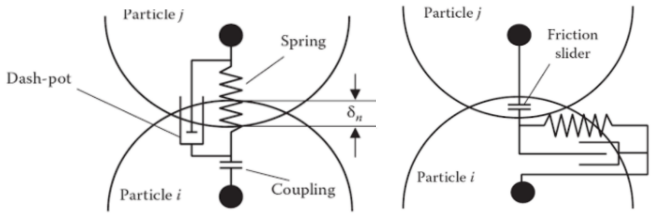

(a) Normal force, $\mathbf{F}_{nij}$ **(b)** Tangential force, $\mathbf{F}_{tij}$

Figure 2.13: Soft sphere model contact force. The figure is adapted from Crowe et al. [25].

The overlap between the two particles is represented as a system of springs and dash pots in both normal and tangential direction. The spring causes the rebound off the colliding particles and the dashpot mimics the dissipation of kinetic energy due to inelastic collisions. In general, deformation of a body will give an energy loss, which depends on the deformation speed. The spring stiffness coefficients, k and the dashpot damping coefficients η are essentially a function of the solid phases the colliding particles belong to [36]. In addition to the spring and dash-pot, there is a coupling and slider feature. The coupling enables to mathematically activate and deactivate the collision model before and after the impact. The slider, on the other hand, describes any effects of sliding friction.

According to the Hertzian contact theory [37] for three-dimensional spheres, the normal force varies as the 3/2 power of the displacement. Therefore, the find relation for the normal component of the contact force, $\mathbf{F}_{nij}$, acting on particle i can be expressed by:

$$\mathbf{F}_{nij} = (-k_n \delta_n^{3/2} - \eta_{nj} \mathbf{G} \cdot \mathbf{n})\mathbf{n}, \tag{2.16}$$

where $\mathbf{G}$ is the velocity vector of particle i relative to particle j, and $\mathbf{n}$ is the unit vector in the direction of the line from the center of particle i to that of particle j. The relation does not take into account the existence of molecular attraction forces [38].

Mindlin extended the Hertz theory by applying a small no-slip frictional tangential force, $\mathbf{F}_{tij}$ across the circular contact area between two spheres that initially are pressed together by a normal contact force, $\mathbf{F}_{nij}$ [39]. The tangential component of the contact force acting on particle i, is given by:

$$\mathbf{F}_{tij} = -k_t \delta_t - \eta_{tj} \mathbf{G}_{ct}, \tag{2.17}$$

where $\delta_\mathbf{t}$ is the tangential displacement vector and $\mathbf{G}_{ct}$ is the slip velocity of the contact point.

For this model, determination of stiffness, k and the damping coefficient η in normal and tangential direction is needed. The normal stiffness k_n can be given using the Hertzian contact theory, given by the following equation when particle i and j have the same radius r, and the same physical properties:

$$k_n = \frac{\sqrt{2r}E}{3(1-\nu^2)}, \tag{2.18}$$

and the tangential stiffness k_t can be given using the Mindlin theory giving the following equation:

$$k_t = \frac{2\sqrt{2}H}{2-\nu^2}\delta_n^{1/2}, \tag{2.19}$$

where H is defined by:

$$H = \frac{E}{2(1+\nu)}. \tag{2.20}$$

The physical properties such as the Young's modulus, E and Poisson ratio, ν are known for a given material. There exist several ways of determining the dampening coefficient. One of the most common ones is that of Cundall and Strack [25], which proposed the following expressions for a particle of mass m that make use of the normal and tangential stiffness coefficients descried above:

$$\eta_n = 2\sqrt{mk_n} \tag{2.21a}$$

and

$$\eta_t = 2\sqrt{mk_t}. \tag{2.21b}$$

These two equations demonstrate critical damping condition, so that bouncing motion after collision is damped as soon as possible.

Hard Sphere Model

The hard sphere model, in contrast, is based on the integrated forms of the equations of motion, namely the impulsive equation. The equation is obtained by time integrating the forces acting on particles assumed to be rigid non-deformable, $\mathbf{J} = \int \mathbf{F} dt$. Solving the impulse equations and applying the concepts of a coefficient of restitution for energy loss and the Coulomb's law of friction yields an explicit relationship between the pre- and post-collisional velocities. In contrast to the soft-sphere model, this model does not resolve the temporal states of the particles.

The hard sphere model is much more computationally effective than the soft sphere model, but it can not handle problems with collisions of three or more particles, or problems in which particles remain in contact for a prolonged time period. For this reason, only the soft-sphere DEM model is suitable for problems with particle adhesion and cohesion [30]. However, Kosinski and Hoffmann [40, 41, 42] showed that this was, in fact, possible by introducing an extended hard-sphere model, but this is not a subject of this thesis.

2.4.5 Modelling the Dispersed Phase

The computational method, DEM used in this thesis solves the equation of motion for each particle by solving the linear and angular momentum equation subject to forces and torques arising both from particle interactions with each other and those imposed on the particles by surrounding fluid.

The conservation equation of linear momentum for a DEM particle of mass m_d can be defined by:

$$m_d \frac{d\mathbf{v}}{dt} = \sum \mathbf{F}, \tag{2.22}$$

where $\mathbf{v}$ denotes the instantaneous particle velocity. There are many force contributions to the particle equation of motion [33], and the most relevant for this thesis is shown in the following:

Drag Force, $\mathbf{F}_{dr}$

Drag is the force component in the flow direction exerted by the fluid on the solid element. According to the Newton's third law of motion, an equal but opposite net force is exerted by the particles on the fluid. There are to two contributions to drag, the component of wall shear, τ_w and fluid pressure acting normal to the wall as shown in Fig 2.14.

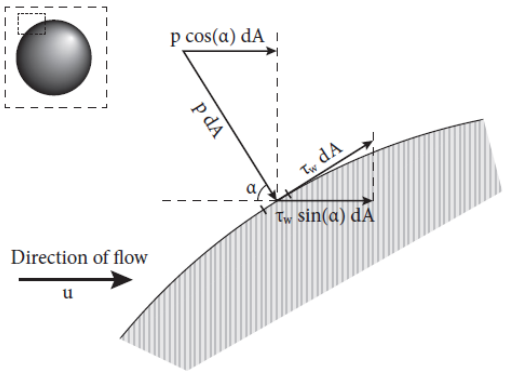

Figure 2.14: Illustration of pressure and shear force acting on an immersed element of area dA inclined at an angle, $\alpha = 90°$ to the direction of the flow [26].

The total drag on the spherical object illustrated in Fig. 2.14 is the sum of the integrals of these quantities over the entire surface. The total integrated drag from wall shear is called wall drag, and the total integrated drag from pressure is called form drag [43]. Drag depends on the properties of the fluid, the size and shape of the object, and the relative velocity between the continuous fluid and the object.

Lift Force, $\mathbf{F}_l$

Lift forces on a particle are due to particle rotation, caused by a velocity gradient or from some other source such as particle contact and rebound from a surface [25].

Particle shear lift force, $\mathbf{F}_{ls}$ applies to a particle moving relative to a fluid, where there is a velocity gradient in the fluid orthogonal to the relative motion as shown in Fig. 2.15.

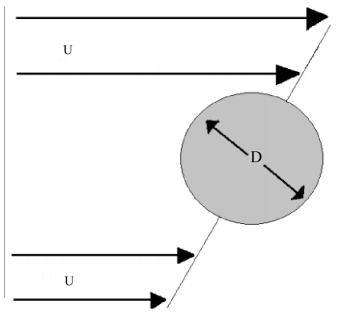

Figure 2.15: Illustration of a particle in a shear flow. The higher velocity on the top of the particle gives rise to low pressure, and the high pressure on the low velocity side gives rise to lift force. The figure is adapted from [25].

Another lift force is the particle spin lift force, $\mathbf{F}_{lr}$, which applies to a spinning particle relative to a fluid as illustrated in Fig. 2.15. When a particle rotates in a fluid, the lift is caused by a pressure differential between both sides of the particle resulting from the velocity difference due to the rotation. The rotation may be caused by other sources than the velocity gradient in the fluid.

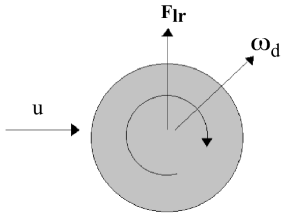

Figure 2.16: Illustration particle spin lift force, $\mathbf{F}_{lr}$, on a rotating particle of angular velocity, ω_d [25].

Contact Force, $\mathbf{F}_{co}$

The DEM phase interaction model, determine how particles behave when they come into contact with each other or solid boundaries. The model is used for describing the particle-particle and particle-wall interactions. The DEM phase interaction model provides access to other models, such as the Hertz-Mindlin model and the linear cohesion model. The contact between two particles is described as the sum of the normal component and the tangential component of the force:

$$\mathbf{F}_{co} = \mathbf{F}_n + \mathbf{F}_t \tag{2.23}$$

The basic Hertz-Mindlin contact model described in section 2.4.4 does not take into account the inter-molecular attraction forces. The linear cohesion model is an extension to facilitate simulation of inter-molecular attraction forces [38], i.e. van der Waals forces, between particle surfaces. They contribute to the progress of aggregating smaller particles into larger particles and to particle deposition on surface materials. This variant of cohesion modelling can use either the Johnson-Kendall-Roberts (JKR) model or the Derjaguin-Muller-Toporov (DMT) model. The cohesion force,F_{coh} between two spherical particles, is expressed in both cases as:

$$F_{coh} = R_{min} W_{coh} \pi f_b, \tag{2.24}$$

where R_{min} is the minimum radius of surfaces in contact, W_{coh} is work of cohesion and f_b is a multiplication model blending factor, with value 3/2 for the JKR model and 2 for the DMT model [33]. The principal difference between these two model formulations is the surface where the cohesion force acts. In the JKR model, this area is limited to direct contact, while in the DMT model it also incorporates the "neck" area in the immediate contact. The JKR model works well for soft materials with relatively high surface energy, while the DMT model is more appropriate for hard solids with low surface energy [44].

Chapter 3

Literature Survey

In order to understand the mechanism of hydrate agglomeration and deposition in flowlines, researchers have performed several studies on adhesion/cohesion force between hydrate particles. This section provides an overview of some relevant hydrate cohesion/adhesion experiments performed under high pressure and low pressure, as well as an overview of hydrate agglomeration and deposition studies performed both experimentally and numerically.

3.1 Experimental Investigation of Hydrate Adhesive and Cohesive Forces

Jung et al. [45] measured adhesive and cohesion forces of hydrates containing various guest molecules (CO_2, CH_4 and tetrahydrofuran (THF)) to surface minerals of mica and calcite, under relatively high pressure and low temperature. A cylindrically shaped hydrate was placed between two parallel mineral plates, one that imposed a pull-out motion and the other measuring a pull-out force. Debonding failure was observed for all the hydrates when mica was the substrate, while in the case of calcite as the substrate, tensile failure was observed for CO_2 and CH_4 hydrates (see Fig. 3.1). In the case of tensile failure for CO_2 and CH_4 hydrates, cohesion force was measured instead of hydrate adhesion force to calcite. It could be shown that hydrate cohesive forces are slightly larger then hydrate adhesive force to mica and calcite mineral surfaces.

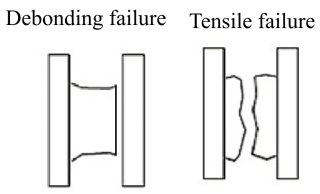

Figure 3.1: Illustration of hydrate debounding and tensile failure adapted from Jung et al. [45]

Groisman et al. [46] determined adhesive strength of hydrates in shape of a disk per unit with use of electrodynamic and gas piston adhesiometers. Both adhesiometers were made in two versions, one used a normal pull-off method and the secound one used a shear method. THF and a mixture of freon-12 (F-12) and natural gases were used as hydrate formers and steel, duralumin and polytetrafluoroethylene (PTFE) were the surface materials investigated. Hydrate formers used in this experiment (THF and F-12) are not naturally occurring components of gas hydrate like CO_2 and CH_4. Hydrates like these are referred to as model hydrate in contrast to real hydrates made of naturally occurring components. Model hydrates are stable at relatively high pressure and low temperature, and for these reasons, they are easy to handle experimentally, but they will represent an error when compared to real hydrates. From the data presented it follows that adhesive force depends on temperature, its value increases sharply with increased subcooling for hydrophilic surfaces and slightly changes for hydrophobic surfaces. Here subcooling is defined as the difference between the equilibrium temperature of the hydrate and the experimental temperature. This observation is in contradiction to the results obtained by Nicolas et al., Yang et al., Dieker et al. and Taylor et al. [47, 48, 49, 50] but in accordance with the result obtained by Klyusov et al. [51].

Klyusov et al. [51] experimentally investigated the adhesion force of natural gas hydrates to steel and copper surfaces of various roughness. Hydrate was formed by moisture condensation on a relatively cold metal cylinder under the study. The hydrate layer was sheared off by a shearing element, and the shear stress was registered (see Fig. 3.2). Also according to these experiments, the adhesive force increase with increased subcooling. The increase was most significant for copper, which is the most hydrophilic material with the highest surface energy tested.

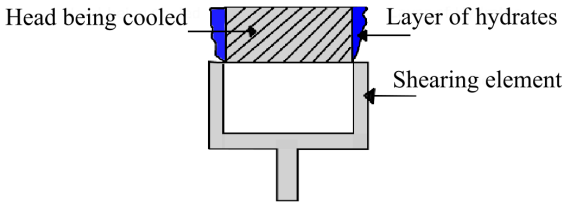

Figure 3.2: Illustration of hydrate shear force measurment adopted from Klyusov et al. [45].

Due to the high roughness of steel and copper (~ 0.335 μm for unpolished and ~ 0.025 μm for polished [52]), van der Waals force which acts on nanometre scale will not be current at such large distance. For this reason, it is assumed in this thesis that the shearing element cuts through the hydrate layer as shown in Fig. 3.3.

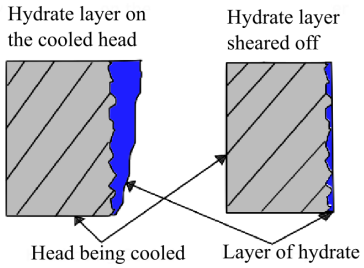

Figure 3.3: Illustration of the shearing element cutting through the hydrate layer.

A much used technique for hydrate force measurements is the micromechanical force apparatus (MMF). The method is performed under both low and high pressure, where the high pressure is advantageous because it allows for the use of real hydrates. However, most previous studies reporting the cohesive/adhesive force of hydrate particles have been done using liquid hydrate formers such as cyclopentane (CyC5) or tetrahydrofuran (THF) due to their ease of use at atmospheric pressure conditions. CyC5 is described by Nicolas et al. [47] as a more suitable model hydrate than THF since CyC5, like naturally occurring hydrate formers, is immiscible in water.

MMF adhesion force measurement is done in a four-step procedure shown in Fig. 3.4. In the first step, the surface sample fixed on a movable cantilever is brought into contact with the hydrate particle on a stationary fibre. Second, the surface sample is held on the hydrate particle with a preloaded displacement, ΔP_{dis}. Third, the surface sample is moved up with a constant velocity until the surface and particle break apart. Last, the maximum displacement of the fibre, ΔM_{dis} is measured and multiplied by the spring constant (k) of the static cantilever to obtain the adhesive force according to the Hooke's law [53]:

$$F = k \cdot \Delta M_{dis} \tag{3.1}$$

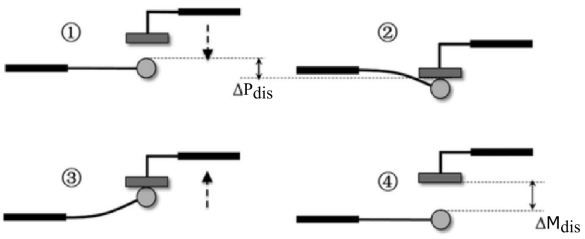

Figure 3.4: Procedure of MMF adhesion force measurement [53].

The procedure of cohesion force measurements is very similar to that of the adhesion force measurement shown in Fig. 3.4. The only difference is that the surface sample is replaced by another hydrate particle as shown in Fig. 3.5.

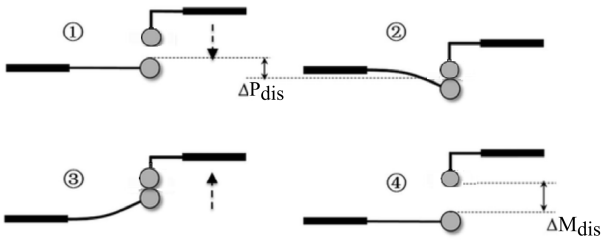

Figure 3.5: Procedure of MMF cohesion force measurement. The figure is adapted from Wang et al. [53].

Aspenes et al. [54] investigated adhesion forces between CyC5 hydrates and solid surfaces, as a function of the solid surface material and the presence of free water. Their results show that the adhesive force between hydrate and the solid surface depends on the surface material. Materials with low surface free energy lead to the lowest adhesion forces. The adhesion force was also strongly dependent on the presence of water in the system. Water drops deposited on the surface strongly increased the adhesion force, and water in the bulk phase increased the hydrate cohesion force.

Nicolas et al. [47] measured the cohesive force between CyC5 hydrates and the CyC5 hydrate adhesive force to a carbon steel (CS) surface in liquid CyC5. A low-pressure MMF apparatus was used, and it was found that the hydrate adhesion force was some lower ($\sim$ 5 times higher) than hydrate cohesion force. The results also show that the measured force, both cohesion, and adhesion was strongly dependent on the subcooling, increasing when the temperature reaches the equilibrium temperature of the hydrate.

Lee et al. [2] applied a high-pressure MMF apparatus to measure cohesion force between CH_4/C_2H_6 (SII) and CO_2 (SI) hydrate particles under high pressure and low temperature conditions in a gas phase. The cohesive force of CH_4/C_2H_6 hydrates was measured as a function of the subcooling and the annealing (hydrate shell growth) time. No apparent temperature dependence of the cohesive force was found, which is in accordance with results obtained by Lee et al. [55], showing no temperature dependence on the hydrate-hydrate cohesion force for hydrate particles annealed for a sufficiently long time.

Wang et al. [53] also applied a high-pressure MMF for cohesion force measurement between CH_4/C_2H_6 hydrate particles and adhesion force measurement to a CS surface. Experimental results indicated that a high amount of free water on the carbon steel surface could significantly increase the adhesion force between the hydrate particles and the surface, which also could be a route to hydrate deposition in flowlines. In these experiments, no measurable adhesion force between CH_4/C_2H_6 hydrate particles and carbon steel surface was obtained in a gas dominate system, when there was no free water present. The adhesion force measurements were then performed with a thin water layer on the surface.

3.2 Experimental Investigation of Agglomeration and Deposition

Joshi et al. [5] performed a series of hydrate formation and dissociation flowloop experiments in water and gas systems. The flowlopp was 95 m long with an internal pipe diameter of 9.72 cm. A sliding-van pump was used to circulate the fluid through the loop, temperature and pressure was controlled, and the pressure drop across the pipe, flow rate, fluid density and particle size distribution were measured during the experiment. A schematic of the flowloop is shown in Fig. 3.6.

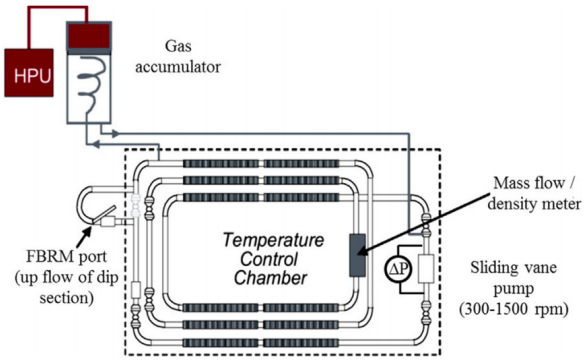

Figure 3.6: Schematic of the flowloop used by Josh et al. [5].

They found that the pressure drop across the flowloop remained almost constant until a certain transition concentration of hydrate, ϕ_{tran}. After reaching this concentration, a rapid increase in the pressure drop was observed, which defines an onset of hydrate plug formation. The effect of mixture velocity, u_{mix} (1 - 2.5 m/s) was investigated. All experiments performed were divided into three different regions. Fig. 3.7 shows the pressure drop across the pump, ΔP as a function of the hydrate concentration, ϕ_d in the water phase.

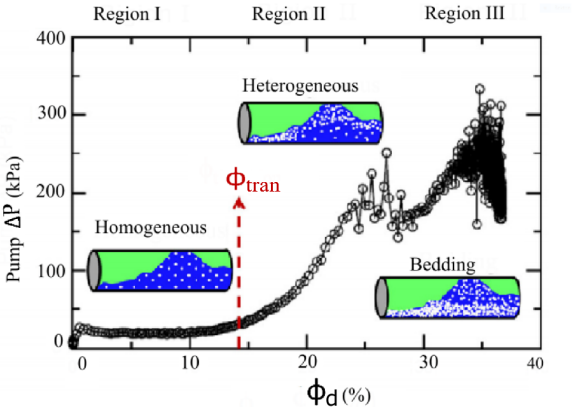

Figure 3.7: Model of methane hydrate plug formation mechanism in 100 vol.% water cut (no oil present) systems. The figure is adapted from Joshi et al. [5].

Fig 3.7 shows that in region I, an increase in ϕ_d does not change the pump ΔP and hydrates where homogeneously distributed. In region II, the pump ΔP increases almost linearly with ϕ_d, and it was observed a transition from homogeneous hydrate dispersion in region I, to heterogeneous hydrate dispersion in region II. Finally, in region III, a substantial increase in pump ΔP with high and large fluctuations was observed, which was attributed to the high resistance from the hydrate bed and wall deposits. Their hypothesis was that the large ΔP observed after ϕ_{tran} results from the formation of gas hydrate bed and wall deposition. The mechanism of hydrate plug formation was proposed starting with transition from homogeneous suspension (region I) to heterogeneous suspension (region II) leading to increased particle interaction and agglomeration, eventually leading to the formation of a hydrate bed and wall deposition (region III). It was found that increased mixture velocity increases ϕ_{tran}.

Aman et al. [6] studied deposition of gas hydrates in oil, water and gas-dominated systems. In the water dominated system, the growth of hydrate film first occurs at the water/gas/pipe interface, leading to hydrate layer formation both above and below the liquid level, see Fig. 3.8. During formation, high shear stress may slug deposits under the liquid level from the wall. The combination of slugging deposits and low relatively solubility of gas in the continuous water phase will tend to restrict the hydrate deposits in the water phase, whereas condensation of water droplets in the gas phase yields a large deposit.

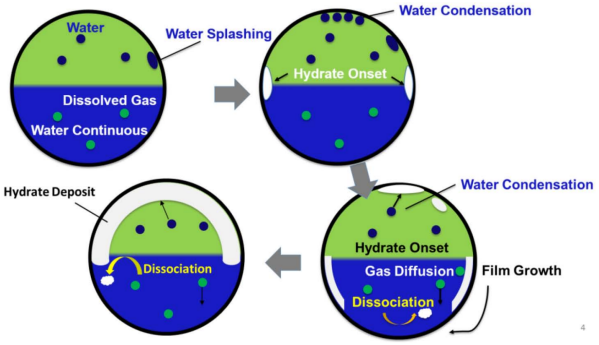

Figure 3.8: Film growth mechanism in water dominated systems [6].

Lippmann et al. [56] performed experiments in a rotating autoclave using a multiphase mixture containing a hydrocarbon gas phase, a hydrocarbon liquid phase, and a water phase, in a pipe made of stainless steel. All experiments show that bigger agglomerates do not adhere to the pipeline wall and no hydrate layer growth took place. For big pipes, the shear force of the slurry seems to be sufficient to prevent hydrate deposition on the pipe wall. All results show that pipeline plugs were caused by high friction from the large amount of hydrate particles, forming a slush mass.

Extensive studies have been performed on ice-water systems with 100 % water cut to investigate the transport properties of ice-water slurries, including mixture velocity and pressure drop investigated by Kauffeld et al. [57]. Four main flow regimes were observed for ice-water flow in a horizontal pipe, as shown in Fig. 3.9. The density of ice (920 kg/m^3 at 0°C) is almost similar to that of methane hydrate (910 kg/m^3), and also lower than that of water (1000 kg/m^3). Hence, ice-water slurries can be used as analogous to hydrate-water slurries.

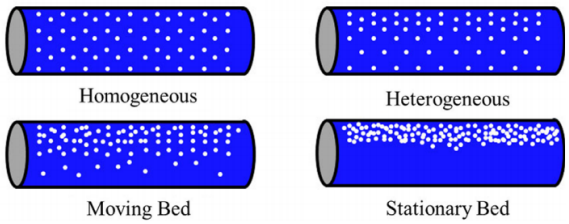

Figure 3.9: Schematic illustration of ice-water slurry flow (ice dispersed in water) [57].

Homogeneous flow regime characterized by uniformly distributed ice particles in the liquid was observed at low solid concentration and high velocities. The pressure drop in the homogeneous flow regime was very similar to that of the carrier fluid phase. When decreasing the velocity and increasing the particle size, a transition to heterogeneous flow was observed, due to buoyant forces. The slurry flow pressure drop increased for higher ice concentration for this regime. Further velocity decrease results in the formation of either moving or stationary bed formation of solid particles, resulting in high slurry flow pressure drop relative to that of the carrier flow.

3.3 Numerical Investigation of Agglomeration and Deposition

Balakin et al. [4] investigated the pressure drop in hydrate slurries, by examining a turbulent flow of gas, hydrates, and water using the CFD two-fluid Eulerian-Eulerian approach. The experimental benchmark for their simulations was taken from the experimental study by Josh et al. [5] described above. According to their results, an onset of hydrate plugging is most probably related the formation of a viscous bed at the gas-slurry interface at hydrate concentration slightly above 15%. In their model, the cohesive force, F_{coh} was set depending on the degree of subcooling, ΔT relative to the hydrate equilibrium temperature. An empirical expression for the cohesion force, F_{coh} was obtained from micromechanical experiments of the cohesion between CyC5 hydrates by Dieker et al. [49]:

$$F_{coh} = \psi \frac{d_0}{2}[0.0017(7.7 - \Delta T) + 0.0007], \tag{3.2}$$

where ΔT is the systems subcooling, the difference between the hydrate equilibrium and experimental temperature, in these simulation set to 7. The original equation, derived for CyC5 hydrates was modified by $\psi \approx 7$ [4], to account for stronger cohesive interactions for high-pressure hydrates of hydrocarbons [58].

A moving bed of hydrate particles was observed to accumulate at the gas-slurry interphase. From these results, it was reasonable to assume that the slug formation starts when the hydrate volume fraction at the gas-slurry interphase rises to a packing limit. However, it was not entirely clear from the results, which mechanism is the most dominant for plug formation. The hydrate adhesive force to the wall material was not set in their model, and for this reason only the effect of increased slurry viscosity on the pressure drop was investigated, showing tolerable discrepancy with the experimental results. They suggested numerical models with high resolution (such as DEM) for further examination of the process of hydrate plugging in high water cut systems.

Hellestø et al. [35] investigated hydrate particle agglomeration in a laminar shear flow of heavy oil using the DEM. The effect of shear rate, γ, dispersed phase loading, ϕ_d, and surface energy, σ was investigated. The terminal agglomerate diameter and number size were shown to decrease with increasing shear rate, the trend flattening out as the shear rate increases. Agglomerates were shown to split into two smaller particle clusters due to the fluid shear force exerted on it. Reduction in the number of particles for the system was associated with longer coagulation time due to the decrease in the amount of inter-particle collision. Four different values of surface energy were tested. The rate of agglomeration was found to be the same throughout the initial (pair-formation) phase for all four values of surface energy. As the system progress into cluster-cluster agglomeration, the rate and the agglomeration efficiency appears to be lower for lower surface energies than the highest surface energy tested, yielding more and smaller agglomerates in the steady-state. However, the number of agglomerates for the lowest surface energy proved, $\sigma = 0.00726$, continuous to grow and flattens out at an elevated steady level without showing any drop in the number of agglomerates due to a cluster-cluster agglomeration. This observation may indicate that the cohesive force is insufficient to support the formation of stable, larger agglomerates. It may be that it exists a threshold magnitude of the surface energy below where stable cluster-cluster agglomeration no longer occurs, expected for their system to be located somewhere in the surface energy range $\sigma \in [0.00762, 0.04191]$ J/m^2. It was found that the lower surface energies, effectively making the agglomerates more susceptible to the flow pattern, yield more chain-like agglomerates of lower densities.

From this literature survey, it was found that uncertainties are associated with the hydrate forces that have been used in previous numerical simulations. An estimate of hydrate-hydrate cohesion forces has been made based on force measurements using model hydrates (Eq. (3.2)), but the hydrate adhesion force to the wall material was not included in the numerical model discussed. However, some research on hydrate forces has been done. Most experiments are investigating the cohesion force between hydrate particles, and just a few experiments have investigated the adhesion force to other surface materials. This thesis focuses on finding a better approximation for hydrate forces, both cohesion and adhesion forces for naturally occurring hydrates, and steel as the surface material based on the experimental findings. Investigation of agglomeration and deposition of gas hydrates dispersed in water has previously been done both experimentally and numerically by the two-fluid Eulerian-Eulerian model. From the experimental investigation, pipeline plugging was attributed to the high resistance from the hydrate bed and wall deposits. Whereas from the numerical investigation, the most probable mechanism was found to be increased slurry viscosity due to hydrate bed formation at the gas-slurry interphase, which potentially could lead to slugging. For further investigation, a high resolution model was recommended. This thesis, therefore, makes an effort to describe the mechanism of hydrate plugging using DEM.

Chapter 4

Methodology

In this chapter, the numerical set-up used for the simulations is shown. First, section 4.1 shows the methodology for converting hydrate adhesive/cohesive forces to work of adhesion/cohesion in the numerical system. Finally, section 4.2 shows the methodology for investigating whether hydrate agglomeration and deposition occur in high water cut pipe systems. The domain geometry and overall system is described before addressing numerical models, process parameters and the simulation procedure.

4.1 Methodology for Simulation of Hydrate Adhesive/Cohesive Forces

In STAR CCM+ particle interaction forces are defined by work of cohesion between similar materials and work of adhesion between different materials. From experiments, contact forces are measured, and this forces must be converted to work of cohesion/adhesion, which are done in these simulations.

4.1.1 Geometry and Mesh

For this simulation, a three-dimensional block geometry of the size $0.01 \times 0.01 \times 0.01$ m^3 was selected. This part was used to provide wall boundaries for injected particles. When a geometry has been specified, a mesh for the flow field can be set. The "trimmer" volume mesh which produce a hexahedral mesh uniformly sized throughout the domain and the surface remesher was selected. The grid base size was set to 0.0012 for this simulation. No fluid flow effects were taken into account, but the computational software requires use of a computational mesh anyway.

4.1.2 System Description

The three-dimensional system, in which the particle-particle and particle-wall interaction were numerically investigated, was defined by a block consisting of no-slip walls containing a cohesive particle (see Fig. 4.1) under influence of a contact force to the wall and a gravitational force.

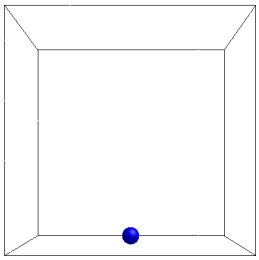

Figure 4.1: Illustration of the spherical particle simulated in STAR CCM+ dispersed in air defined by four impermeable walls.

4.1.3 Models and Solvers

The physical models in STAR CCM+ decide the behaviour of the material investigated, by defining the physical phenomena considered, and by defining the mathematical formulations and conditions. They work together with the solver to obtain a solution. Table 4.1 summarizes the most important models and solvers used in this part of the thesis.

Table 4.1: Physical models and solvers in STAR CCM+ used for this simulations.

Solvers	Implicit Unsteady, Lagrangian Multiphase, and DEM Solver
General models	DEM, Lagrangian Multiphase, Gravity, Implicit Unsteady, Multiphase Interaction, and Three-Dimensional
Lagrangian models	Constant Density, DEM Particles, Solid and Spherical Particles
Interaction models	DEM Phase Interaction, Hertz-Mindlin and Linear Cohesion (JKR)

The Lagrangian multiphase model was activated to create the dispersed hydrate phase within the simulation. Each Lagrangian phase contains a boundary conditions manager node to define the solid wall material, which the particle may come in contact with.

The numerical method used to simulate the motion of hydrate particles was the DEM, and the Lagrangian phase was then represented by DEM particles of constant density. The method demands significant computer power that results

in detailed resolution that other method can not achieve. DEM is an extension of the Lagrangian modelling methodology, including inter-particle contact forces in the particle equation of motion [33]. The basic Hertz-Mindlin contact model was chosen, in addition to the linear cohesion model to simulate inter-molecular attraction (van der Waals force) between surfaces. The cohesion model works in tandem with the contact model, both contact and cohesion works simultaneously when a particle attaches [33]. The implicit unsteady time model was chosen in order to investigate the temporal behaviour of the solid particle.

The solvers in STAR CCM+ controls the solution and are activated once per iteration. The models elect the required solvers, and different models can use the same solver and sometimes one model needs more than one solver. The DEM solver was used to enable tracing of each particle element and the implicit unsteady solver was primarily used to control the update at each physical time-step in addition to controlling the size of each time-step.

4.1.4 Particle Injector

In STAR-CCM+, particles can enter the fluid continuum through different injectors. The Lagrangian phase defines what particles that would enter the domain and how they behave, while the injector defines the direction and the frequency of particle flow into the system. Different types of injectors were available, which allows for particle injection in different ways; randomly, from a surface or from a specific point. For this simulation, the particle was injected at a specific point close to the bottom wall. After the particle was injected, the injector was deactivated to prevent more particles from being injected.

4.1.5 Process Parameters

A key selection of process parameters for both the dispersed phase and the boundary walls are represented in table 4.2.

Table 4.2: Process parameters.

Material	Process Parameters	Value	Unit
Dispersed phase	Particle size, D	$8{\cdot}10^{-4}$	m
	Density ρ_d	(910/940)	kg/m^3
	Poisson ratio, ν	0.31	-
	Young‘s modulus, E	$8.7{\cdot}10^{9}$	Pa
	Static friction coefficient	0.62	-
Wall	Density	7832.0	kg/m^3
	Poisson ratio, ν	0.285	-
	Young‘s modulus	$2.0{\cdot}10^{11}$	Pa
	Static friction coefficient	0.46	-

The particle size, D was set to 0.8 mm, representing an aggregate some larger than the elementary particle size. The dispersed phase was set to have a Young's modulus of $E = 8.7$ GPa and a Poisson ratio of $\nu = 0.31$, which are the values for ice. The hydrate density was set to 910 kg/m^3 for CH_4 hydrates (SI) and 940 kg/m^3 for CH_4/C_2H_6 hydrates (SII), and the wall material was set to carbon steel.

4.1.6 Simulation Procedure and Calculations

After injecting the hydrate particle to the system, a small gravitational acceleration of 9.81 m/s^2 was set to act on the particle in the negative y-direction to connect the particle to the wall (see Fig. 4.2). The particle velocity decreased to almost zero ($\sim 1{\cdot}10^{-14}$ m/s), when a sufficient contact was achieved. After this step, a gravitational acceleration corresponding to the experimental measured forces was set to act on the particle in the positive y-direction to detach the particle from the wall (pull-off) or turned to the positive x-direction to shear off the hydrate particle (shear) from the wall.

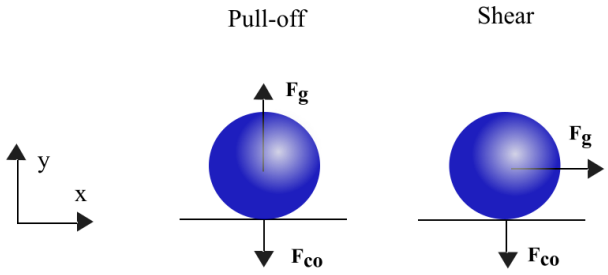

Figure 4.2: Illustration of the cohesive/adhesive particle simulated in STAR CCM+, in contact with a wall material. Gravitation force, $\mathbf{F}_g$ and contact force, $\mathbf{F}_{co}$ work on the particle.

The magnitude of the gravitational acceleration was calculated by dividing the adhesion/cohesion contact force found for the simulated system, F_{sp}, corresponding to the experimentally measured force, by the mass of the simulated hydrate particle. Adhesion and cohesion force data were derived from different experimental set-ups (particle-particle, particle-plate, cylinder-plate, etc.), therefore the results are not directly comparable. The simulations were performed for the particle-wall system, and for this reason, the experimental forces were converted to the corresponding force for this simulated system through calculation of the Hamaker constant. Eq. (2.8) was used for this calculations, an overview is presented in Appendix B.

The work of cohesion/adhesion in the model was set to a high value and gradually reduced until the particle detach from the wall. Hydrate detachment was defined by particle velocity exceeding $1{\cdot}10^{-5}$ m/s. For hydrate work of cohesion measurements, both the wall and the particle material was set to have hydrate

properties. For hydrate work of adhesion measurements to carbon steel, the particle was set to be hydrate and the wall material was set to be carbon steel.

4.2 Methodology for Simulations of Hydrate Agglomeration and Deposition

4.2.1 Geometry and Mesh

The geometry chosen for these simulations was based on a three-dimensional pipe containing dispersed hydrate particles in water with the following parameters: particle radius, $R = 0.4$ mm, particle volume fraction, $\phi_d = 0.3$, pipe height containing liquid water, $H_p = 7.29$ cm and number of particles, $n = 50\,000$. The experimental benchmark for this simulations was taken from the comprehensive study performed by Joshi et al. [5], and the numerical set up was inspired by the simulations performed by Balakin et al. [4] and Hellestø et al. [35]. In this thesis, the experimental three-dimensional system (see Fig. 4.3) was replaced by a two-dimensional system, for the purpose of reducing the simulation time. It was then necessary to calculate the corresponding two-dimensional parameters from three-dimensional ones. An equivalent two-dimensional solid fraction was chosen so that the the average three-dimensional inter particle spacing $C = (4\pi/3\phi_d)^{1/3}R$ was equal to the average two-dimensional spacing $C = (\pi/\alpha_d)^{1/2}R$ [59]. The equivalent formula is thus given by:

$$\alpha_d = (\frac{3\sqrt{\pi}\phi_d}{4})^{2/3}. \tag{4.1}$$

Eq. (4.1) yields the area fraction, α_d, equal to 0.542. The area fraction is defined as the area of particles in the system divided by the total area of the system, and from that, the length of the two-dimensional rectangle was estimated to be $L_p = 0.6361$ m. STAR CCM+ is a three-dimensional based tool, and a 3D-CAD model is generated by sketching this pipe in the xy-plane, extruded it to create a body, and then convert it to a two-dimensional domain.

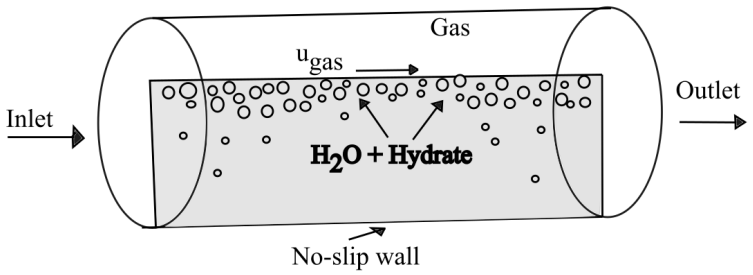

Figure 4.3: Illustration of the experimental flow system used as benchmark for this simulations. Water and hydrate account for 75% of the pipeline volume, while the gas occupies the remaining 25% volume on the top.

The same surface and volume mesh as described in section 4.1 was used in this simulation. The grid base size was set to 0.0012, corresponding to a 530 $\times$ 61 cell system for the 0.6361 m $\times$ 0.0729 m simulation domain.

4.2.2 System Description

The 2D simulation domain consists of two non-permeable no-slip walls: a moving top wall, and a stationary bottom wall. The left side was set to velocity inlet and the right side to pressure outlet. The moving top wall and the velocity inlet introduced a shear flow that efficiently brings dispersed particles in contact with other particles and the walls. The low relative velocity yielded fast agglomeration and deposition of cohesive particles. Two types of systems were under study: case 1 with an internal interfaces set to periodic (PBC) at the right and the left side in addition to velocity inlet at the left side and pressure outlet at the right side, and case 2 with just velocity inlet at the left side and pressure outlet at the right side. The reason for introducing periodic boundaries is to mimic an infinite simulation domain. This means that flow parameters (mass, momentum, and energy) leaving through one boundary will be introduced in the other one. Therefore, it is possible to run the simulation for as long as necessary and still have the same content of material under investigation. Fig. 4.4 shows the simulated system for case 1.

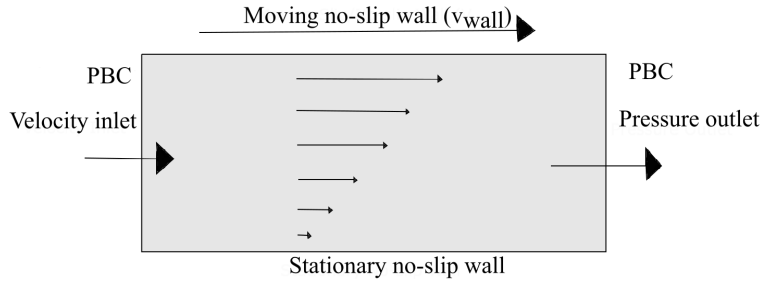

Figure 4.4: Illustration of the simulated flow system. The moving top wall and the velocity inlet induce a shear-flow, which yields a velocity profile within the domain.

Therefore, couette flow-like systems were obtained. The velocity profiles in the middle of the pipe in x-direction plotted against the vertical y-direction of the pipe for the two cases are demonstrated in Fig. 4.5. The objective was to simulate experiments in which there was gas on the top of the water phase, as shown in Fig. 4.3. In CFD simulations it is computationally expensive to specify the top wall as a gas phase (i.e VOF technique) and model DEM particles at the same time. The upper boundary was also made cohesive in order to account for the capillary interactions at the interphase which capture the particles.

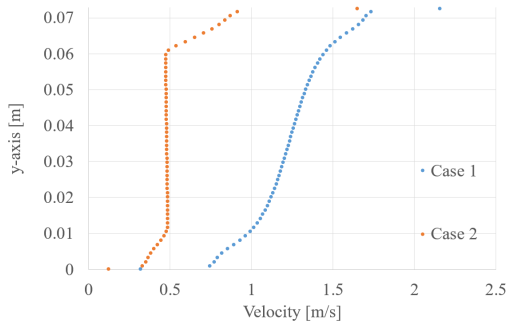

Figure 4.5: Illustration of fluid velocity fields with (case 1) and without PBC (case 2).

The y-axis is defined to be in the same direction as the vertical hight of the simulated pipe and the x-axis to be in the same direction as the horizontal length of the simulated pipe.

4.2.3 Models and Solvers

Table 4.3 summarizes the most important models and solvers used in this simulations.

Table 4.3: Physical models and solvers in STAR CCM+ used for this simulations.

Solvers	Implicit Unsteady, Lagrangian Multiphase, DEM Solver, Coupled Implicit and K-Epsilon Turbulence
General models	Constant Density, Coupled Flow, DEM, Gravity, Implicit Unsteady, K-Epsilon Turbulence, Lagrangian Multiphase, Liquid, Multiphase Interaction, Turbulent and Two-Dimensional
Lagrangian models	Constant Density, DEM Particles, Drag Force, Shear Lift Force, Solid, Spherical Particles, Spin Lift Force, Turbulent Dispersion and Two-Way Coupling
Interaction models	DEM Phase Interaction, Hertz-Mindlin and Linear Cohesion (JKR)

There are many common features with the models described in section 4.1.3, but the models used in this section is somewhat more comprehensive. The two-dimensional continuum consists of two phases: liquid water and hydrate parti-

cles. The flow regime was turbulent, due to the low fluid dynamic viscosity and corresponding high Reynolds number. The k-ε turbulence model was selected.

Particle interaction was of special interest, and for this reason also in this simulation, the Lagrangian DEM model was chosen. Drag force, pressure gradient force, shear lift force, spin lift force and gravitational force were included in the Lagrangian model to determine the phase interactions (see Fig. 4.6). The gravitational force will, in this case, contribute to additional contact between the dispersed particles due to buoyancy, which is a result of the hydrate phase being lighter than the continuous fluid phase.

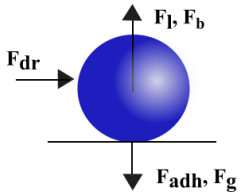

Figure 4.6: Illustration of the force balance on a particle in contact with a wall. Drag force $\mathbf{F}_{dr}$, adhesion force $\mathbf{F}_{adh}$, gravitation force $\mathbf{F}_{g}$, lift force $\mathbf{F}_{l}$ and buoyancy $\mathbf{F}_{b}$ all act on the particle.

The Hertz-Mindlin basic contact model and the linear cohesion model were selected due to investigate the ability of inter-molecular van der Waals force to form agglomerates and deposits, which may potentially lead to plugging. The two-way coupling model was chosen to enable the particle phase to influence the continuous phase flow, which becomes important for high particle loadings as in this case.

The DEM solver was used to enable tracing of each of the $\sim$ 50 000 particle elements. The DEM solver is in this way opposite to the traditional DPM solver, which indeed is a Lagrangian tracker, but with the drawback of parcel treatment (see section 2.4.3). DEM uses a soft-sphere approach to model particle contact, which allows for the inclusion of cohesive force. The DPM solver, on the other hand, uses a hard-sphere approach which is unsuitable for modelling agglomeration and deposition (see section 2.4.4). The simulation was first set to be one-way coupled, and changed to two-way coupled after achieved stable maximum agglomerate size.

The flow specification can either be segregated or coupled. In this thesis, the flow specification follows the coupled flow model. The coupled flow model solves the conservation equation for mass, momentum, and energy simultaneously in contrast to the segregated flow model were they are solved separately. The implicit unsteady time model was chosen in order to investigate the temporal behaviour of each particle.

4.2.4 Particle Injector

Two types of injectors were used, depending on the boundary conditions, either the surface injector or the random injector introduced the dispersed phase to the domain as illustrated in Fig. 4.7.

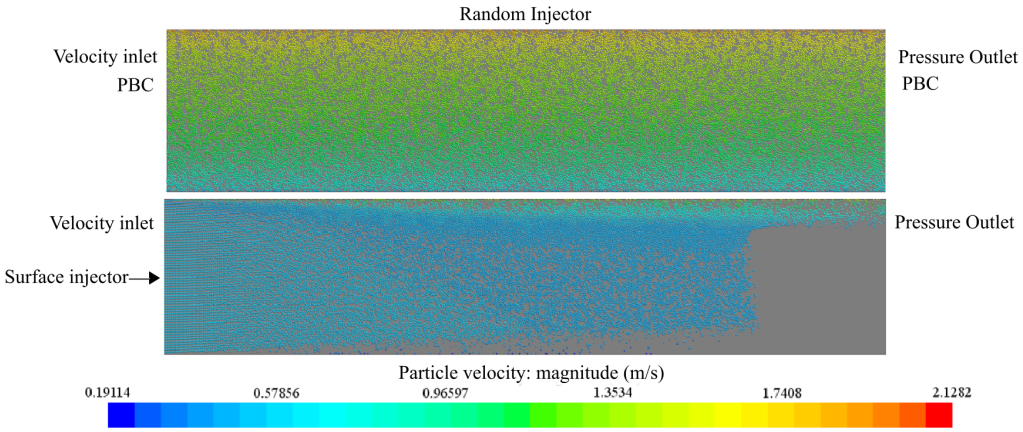

Figure 4.7: Illustration of the two types of injectors used, random and surface injector, and the boundary conditions used.

The random injector was used to fill the simulation domain with hydrate particles in the case of periodic boundary conditions. This special injector type for DEM particles injects 50 0000 particles into the region with a random point distribution during eight iterations of time step 0.1 s, giving a unique starting point for each simulation. In the period of injection, particle interactions were set to be zero.

For simulation domains without periodic boundary conditions, the surface injector was used. Particles were set to be injected from the left surface by a particle flow rate, $\dot{p} \sim 2500000$ particles/s, calculated from the process parameters presented in Table 4.4. First, the volume flux, Q_d has to be calculated:

$$Q_d = \overline{u} \cdot A_p \cdot \phi_d, \tag{4.2}$$

where $\overline{u}$ is the mean velocity in the pipe, equal to the inlet velocity, A_p is the cross section area of the pipe and ϕ_d is the volume fraction of the dispersed hydrate particles in the pipe. To obtain the particle flow rate, $\dot{p}$, the volume flux, Q_d was divided by the volume of the dispersed particle:

$$\dot{p} = \frac{Q_d}{V_d}. \tag{4.3}$$

Even with a very low time step, $5{\cdot}10^{-5}$, the number of particles in the domain did not reach 50 000 particles, but flattened out at about 45 600 particles. This number of particles corresponds to a area fraction, $\alpha_d = 0.494$ and a volume fraction, $\phi_d = 0.261$.

4.2.5 Process Parameters

Table 4.4 shows the most important process parameters used in these simulations.

Table 4.4: Process parameters.

Material	Process Parameters	Value	Unit
Dispersed phase	Particle size, D	$8{\cdot}10^{-4}$	m
	Number of particles (case 1), n	50 000	-
	Number of particles (case 2), n	45 600	-
	Particle density, ρ_d	910	kg/m^3
	Particle-particle work of cohesion, W_{coh}	$6.968{\cdot}10^{-3}$	J/m^2
	Particle-surface work of adhesion, W_{adh}	$0.832{\cdot}10^{-3}$	J/m^2
	Poisson ratio, ν	0.31	-
	Young's modulus, E	$8.7{\cdot}10^{9}$	Pa
	Static friction coefficient	0.62	-
	Particle volume fraction (case 1), ϕ_d	0.30	-
	Particle area fraction (case 1), α_d	0.524	-
	Particle volume fraction (case 2), ϕ_d	0.26	-
	Particle area fraction (case 2), α_d	0.494	-
Continuous phase	Fluid density, ρ_c	1003	kg/m^3
	Fluid dynamic viscosity, μ_c	$1.60{\cdot}10^{-3}$	Pa s
	Velocity inlet, u_{in}	0.51	m/s
Wall	Top wall velocity, v_{wall}	2.47	m/s
	Density, ρ_w	7832.0	kg/m^3
	Poisson ratio, ν	0.285	-
	Young's modulus, E	$2.0{\cdot}10^{11}$	Pa
	Static friction coefficient	0.46	-

The molecular properties of water and gas hydrates are given under experimental conditions ($P = 6.89$ MPa and $T = 269.77$ K) in table 4.4 [5]. The inlet velocity, u_{in} was defined according to Balakin et al. [4] assuming that the experimental pressure gradient of 44.2 Pa/m (time-average) in the case of no hydrate condition was equal in the gas and liquid phase. In addition, the gas flow velocity u_{gas} was specified as the tangential component of boundary velocity at the top wall:

$$v_{wall} = \frac{(u_{mix} - \phi_w \cdot u_{in})}{(1 - \phi_w)}, \tag{4.4}$$

where ϕ_w is the volume fraction of the continuous water phase and $u_{mix} = 1$ m/s is the mean velocity of the gas-liquid flow, reported in the experimental work [5]. The continuous phase was set to liquid water, and the wall material was set to carbon steel. The number of dispersed particles was set to 50 000 in case 1 and about 45 600 for case 2. The work of cohesion/adhesion was set in accordance to the numerical results from the simulations described in section 4.1.

4.2.6 Simulation Procedure

At first, the simulations were run without particles in the system. The initial velocity was set to zero, so that the only influencing parameter at start-up was the moving top wall and the velocity inlet boundary. The goal of these first step was to achieve a steady state velocity profile. When this was obtained, the fluid flow was set to be independent of time, ready for particle injection which then will constitute a one-way coupled multi-phase flow. Hydrates will experience agglomeration and deposition over time due to contact forces set in the model. After achieving stable maximum hydrate cluster size, the multiphase system was changed to be two-way coupled, meaning that particle impact on the fluid also was taken into account (see section 2.4.1).

4.2.7 Post Processing Tools

The CFD software STAR-CCM+ is a multi-purpose simulation software with post-processing tools. In order to analyze results from the simulations, scenes, reports, plot and solution histories were used.

Scenes were created as visualization displays of the geometry, mesh, scalars, and vectors, allowing for viewing of solution data from either a running or a finish simulation. It is possible to watch a flow field evolve as the simulation iterates, change parameters and immediately see the effects of those changes. Available variables that can be studied are associated with the selected models, when activated a physical model, predefined variables for this model become available. A solution history was created to make a movie of the scenes for the complete simulation. This also makes it possible to look back on scenes at a given time.

The parameters of particular interest for the current work was the agglomerate and deposit size and their geometric structure. When adding the DEM model, it become possible to study the particle connected component size, i.e. agglomerate size in terms of how many particles they contain. This post-processing tool gives then the possibility of evaluating the physical size of the agglomerates and their position. Reports can be used to study changes over time, and other plots can be used to study variations with the height and the length direction in the pipe.

Chapter 5

Results and Discussion

This chapter shows a comparison of hydrate cohesion/adhesion force results from several experiments, as well as discusses the significance of these forces for a multiphase system. The first section discourses experimental force findings, and extract the most relevant data from these. Next, the hydrate work of cohesion/adhesion is numerically measured. Last, the measured work of cohesion/adhesion found for hydrate particles was used to study agglomeration and deposition tendency of hydrate particles in a pipeline systems with high water cut.

5.1 Hydrate Contact Forces

An overview of hydrate-hydrate cohesive forces and hydrate-surface adhesive forces from five different articles are represented in Fig. 5.1.

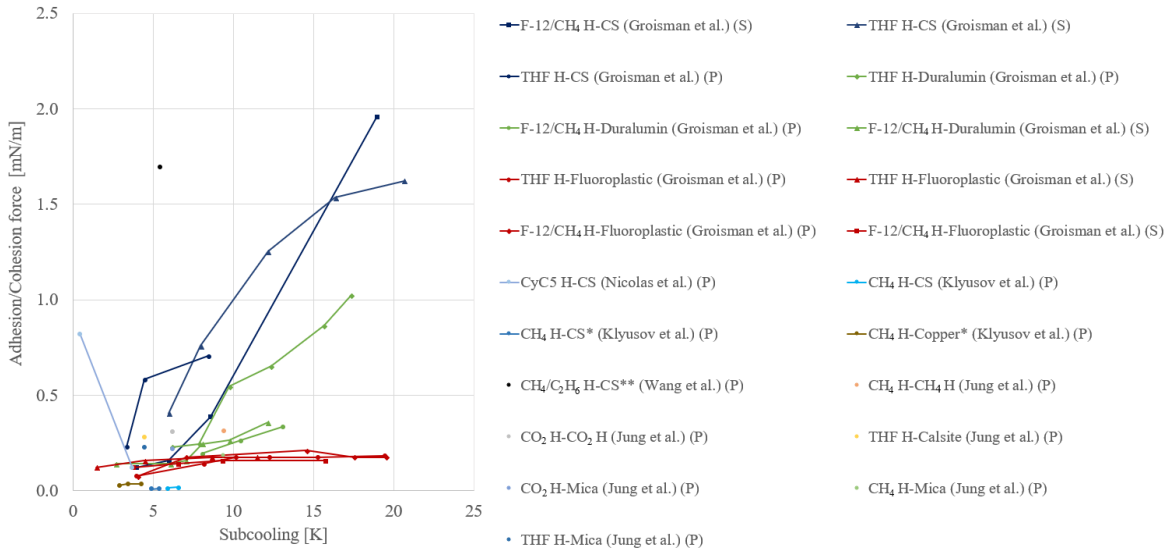

Figure 5.1: Adhesion and cohesion hydrate force plotted against subcooling.

The cohesion/adhesion force of F-12/CH_4, THF, CO_2, CH_4, CH_4/C_2H_6 and CyC_5 hydrates divided by the hydrate particle diameter as a function of the subcooling from their relative equilibrium temperature are given in Fig. 5.1. Shear experiments are denoted by S, pull-off experiments by P, hydrate by H and carbon steel by CS. The asterisk, * indicates polished surface and the double asterisk, ** indicates a thin water layer on the surface.

Jung et al. [45] measured adhesion and cohesion force of SI hydrates, founding that hydrate cohesion forces was somewhat larger than hydrate adhesion forces. The CH_4 hydrate-hydrate cohesion force was almost twice larger than for CH_4 hydrate adhesion force to a mica surface. The greatest force was measured between CH_4 hydrates followed by the cohesive force between CO_2 hydrates.

Groisman et al. [46] performed experiments of the adhesive force of model hydrates using three different surface materials, steel, duralumin and fluoroplastic, mentioned in order from the highest to the lowest surface free energy. The surface material with the highest surface free energy also shows the largest measured adhesion force, which is in accordance with Aspenes et al. [54]. Two different methods for force measurement was used: pull-off and shear method, and it was concluded that the method does not influence the results.

Klyusov et al. [51] measured adhesion forces of natural gas hydrates (CH_4 hydrates) to steel and copper as surface materials using a shear method, finding that the adhesion force was greatest for copper as surface material, which is the material with the highest surface free energy. However, the shear force values obtained by Klystov et al. were significantly lower than adhesion force values obtained by Groisman et al. and Jung et al.

As mentioned in the literature survey, data from Groisman et al. and Klyusov et al. showed increased adhesion forces with decreased temperature/increased subcooling. The increase was most significant for hydrates to the materials with the highest surface energy found by Groismn et al. However, other literature results show the opposite trend, due to the formation of capillary bridge when the hydrate temperature approaches the equilibrium temperature, and the results from Nicolas et al. [47] are a typical example. The adhesion forces were measured at relatively high subcooling values by Groisman et al. A possible explanation for the observed increased force with increased subcooling is that there exists a minimum adhesion force. When increasing the subcooling further from this value, the measured adhesion force will increase. From Fig. 5.1 this subcooling value appears $\sim$ 5 K. However, further experimental research is required in order to get a better understanding.

Lee et al. [2] and Wang et al. [53] measured cohesion force of CH_4/C_2H_6 hydrates using a high pressure MMF apparatus. They found the measured forces to be substantially larger than the cohesion force of CH_4 hydrates measured by Jung et al. Nevertheless, the force measurement by Jung et al. was carried out at a much higher subcooling, and for this reason was less interesting for this research. The cohesion forces measured by Lee et al. and Wang et al. are generally much higher than the force measurements represented in Fig. 5.1, and therefore, these measurements are not shown in the figure.

In addition to the hydrate cohesion force measurements, Wang et al. investigated the CH_4/C_2H_6 hydrate adhesion force to a carbon steel surface with a thin water layer on the surface. The measured cohesion force was found to be much higher than the adhesion force, even with a small amount of free water present on the carbon steel surface surface.

Experimental results obtained by real hydrates, like CH_4 and CH_4/C_2H_6 and carbon steel surface without any free water present, were considered as the most relevant ones for this research. Thus, CH_4 hydrate adhesion force to steel measured by Klyusov et al. was considered as the most relevant cohesion force measurement found. There is a significant uncertainty associated with the assumption made for hydrate adhesion force to steel. Relatively little research has been done in this area, and there is therefore not enough comparison basis. The measurements was performed using a less known shear apparatus. The more recognized pull-off device, the MMF apparatus was not able to measure that low forces. For hydrate-hydrate cohesion force, Jung et al., Wang et al. and Lee et al. make use of real hydrates for cohesion force measurements. However, the cohesion force obtained by Jung et al. was measured with a less recognized device at a very high subcooling, $\Delta T \sim 9.38$, and stands out from the other two with a much lower value. For this reason, it was considered as less interesting for this research.

5.2 Work of Cohesion/Adhesion

In this section work of cohesion/adhesion obtained from numerical simulations based on the most relevant hydrate forces discussed in section 5.1 is shown.

Fig. 5.2 shows work of adhesion and cohesion as a function of the subcooling. The measurments are based on experimental results from Klyusov et al. [51], Wang et al. [53], and Lee et al. [2]. Even though the hydrate adhesion force to steel was experimentally measured to be relatively low, the work of adhesion found by numerical simulations show that the work of adhesion measured with the shear method was only about seven times lower than the cohesion force measured by the pull-off method. The magnitude of the work measured in STAR CCM+ depends therefore on the method used. The same gravitational force measured from experiments results in a higher work value using the shear method than the pull-off method. This indicates that the selection of the

measuring method influences the resulted force. This is in contradiction to the results found by Groisman et al., where the method does not affect the results.

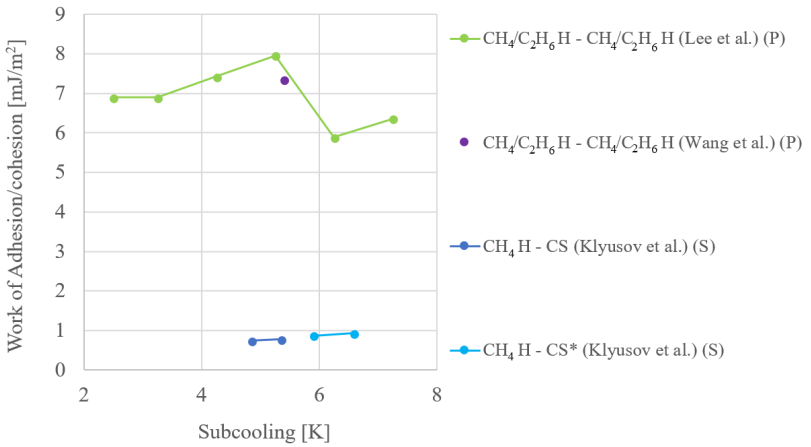

Figure 5.2: Work of adhesion and cohesion of hydrates.

Table 5.1 to 5.3 give the experimental forces, (F_{ss}, F_{sp} or F_{pp}), the corresponding Hamaker constants, A_H, the corresponding force for the simulated system, F_{sp}, gravitation acceleration, g, and the obtained work of adhesion from the simulations, W_{adh}.

Table 5.1: CH_4-CS (CS cylinder diameter 20 mm and hight 10 mm) adhesion force from Klyusov et al. [51]. The asterisk, * indicates that the surface is polished.

Material	F_{pp} [N]	A_H [J]$\cdot 10^{22}$	F_{sp} [N]$\cdot 10^{9}$	g $[\frac{\mathrm{m}}{\mathrm{s}^2}]$	W_{adh} $[\frac{\mathrm{mJ}}{\mathrm{s}^2}]$	ΔT [K]
H-CS*	2.90	1.24	6.53	0.027	0.745	4.85
H-CS*	3.00	1.28	6.74	0.028	0.775	5.35
H-CS	3.40	1.45	7.64	0.031	0.875	5.90
H-CS	4.00	1.70	9.00	0.037	0.935	6.58

Table 5.2: CH_4/C_2H_6 hydrate-CH_4/C_2H_6 hydrate (hydrate particle diameter $\sim$ 800 μm) cohesion force from Wang et al. [53].

Material	F_{ss}[N]$\cdot 10^{5}$	A_H [J]$\cdot 10^{19}$	F_{sp} [N]$\cdot 10^{5}$	g $[\frac{\mathrm{m}}{\mathrm{s}^2}]$	W_{coh} $[\frac{\mathrm{mJ}}{\mathrm{s}^2}]$	ΔT [K]
H-H	1.39	5.26	2.78	110.160	7.355	5.4

The CH_4/C_2H_6 hydrate cohesion forces obtained by Wang et al. shown i Table 5.2 is in good agreement with the results obtained by Lee et al. shown in Table 5.3.

Table 5.3: CH_4/C_2H_6 hydrate-CH_4/C_2H_6 hydrate (hydrate particle diameter $\sim$ 500 μm) cohesion force from Lee et al. [2].

Material	F_{ss} [N]$\cdot 10^6$	A_H [J]$\cdot 10^{19}$	F_{sp} [N]$\cdot 10^5$	g [$\frac{m}{s^2}$]	W_{coh} [$\frac{mJ}{s^2}$]	ΔT [K]
H-H	8.12	4.93	2.60	103.176	6.895	2.50
H-H	8.12	4.93	2.60	103.176	6.895	3.25
H-H	8.75	5.31	2.80	111.112	7.425	4.25
H-H	9.37	5.68	3.00	119.049	7.955	5.25
H-H	6.94	4.21	2.22	88.096	5.885	6.25
H-H	7.50	4.55	2.40	95.239	6.365	7.25

An average value of results based on hydrate-hydrate cohesion force by Wang et al. and Lee et al. was considered as a good estimate of hydrate work of cohesion, W_{coh} = 6.968 mJ/m^2. Whereas, an average value of results based on hydrate adhesion force to steel by Klyusov et al., W_{adh} = 0.832 mJ/m^2, was considered as a reasonable estimate for hydrate work of adhesion to a carbon steel surface.

5.3 Hydrate Agglomeration and Deposition

In this section, results from two simulations with the purpose of numerically investigating agglomeration and deposition in a horizontal pipeline are shown. The only difference is the boundary conditions: for case 1, PBC are specified at the left and the right side of the domain. For case 2, however, the standard inlet and outlet boundary conditions were used. The results are presented with the help of snapshot of scenes from STAR CCM+ and graphs.

Fig. 5.3 shows the fluid velocity profiles in the two simulated cases.

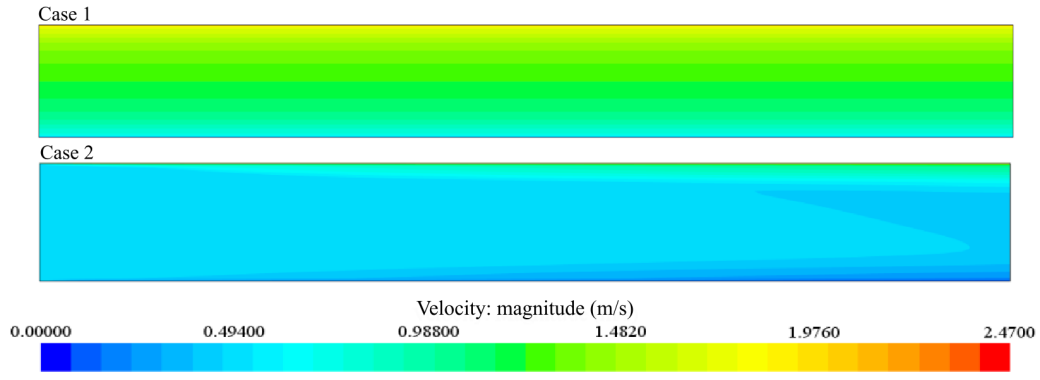

Figure 5.3: Fluid velocity profiles for case 1 and 2 without particles.

Due to the different boundary conditions, the two systems for studying particle agglomeration and deposition do not have the same fluid velocity profile within the domain, as shown in Fig. 5.3. The obtained average velocity was higher

in case 1, than in case 2. In case 1, the average velocity in the middle of the pipe was found to be 1.23 m/s; this value was the same along the pipe length, whereas in case 2 the fluid velocity was found to be 0.54 m/s in the middle of the pipe; this value becomes higher further into the pipe.

5.3.1 Hydrate Agglomeration

The injected particles were transported together with the carrier fluid and they increased in dimension under the flow due to agglomeration. Fig. 5.4 shows the maximum particle connected component size (number of particles connected) as a function of time.

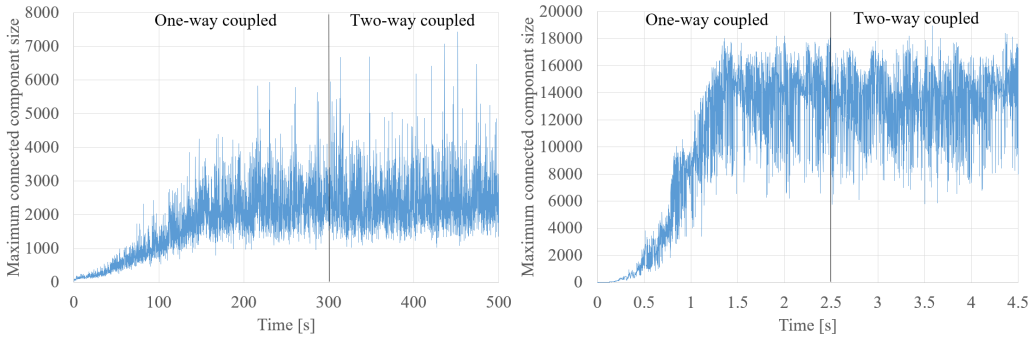

(a) Case 1 **(b)** Case 2

Figure 5.4: Maximum particle connected component size as a function of time.

The terminal particle connected component size was found to be largest for case 2, with a maximum of approximately 19000 particles. In case 1, the maximum particle connected component size was found to consist of approximately 7500 particles. This observation indicates that the higher fluid velocity, which results in a higher shear force on the immersed objects, significantly decreases the maximum agglomerate size.

In case 1, particles were initially homogeneously dispersed in the carrier fluid. The one-way coupling was assumed for the first 300 s. Afterwards, the two-way coupling was selected in the model. The maximum agglomeration size increased from 1 to almost 175 particles during the five first seconds. The agglomerate did not change its size until 25 s, but later it started to grow almost linearly until 175 s. Finally, the size reached the maximum and stabilized at about 2400 particles as shown in Fig. 5.4 (a).

In case 2, particles were injected from the left boundary. The one-way coupling was assumed for the first 2.5 s. Afterwards, the two way coupling was selected in the model. The onset of massive agglomeration started after 0.25 s when about 950 particles were injected into the domain, and the maximum connected component size increased almost linearly from that time and until 1.5 s after particle injection. The residence time of the particles, i.e. the time it

takes for particles to flow through the simulated pipe was then reached. The first injected particles left the pipe at the outlet, and the number of particle in the pipeline stopped to increase. The agglomerate size reached the maximum and flattened out at about 14300 particles as shown in Fig. 5.4 (b).

In both cases, when the curves flattened out, significant fluctuations in the maximum agglomerate size over time occurred due to splitting and regeneration of agglomerates. The large agglomerates that are formed are thus unstable. As shown in Fig. 5.4, the agglomerates appear to be more unstable with increasing size. When introducing the two-way coupling into the model, the maximum connected component size tended to be almost unaffected. Only a some more irregular variation, with larger flocculates in the maximal size was observed for both case 1 and case 2.

Particles moved through the pipe due to the force from the fluid, but also upwards due to the lift forces and buoyancy. The latter forces become essential for the particles motion in case 1 because the same particle material was studied over a longer time period, allowing these forces to affect the particles significantly. Fig. 5.5 shows the maximum particle connected component size at four different times when the one-way coupling was selected in the model.

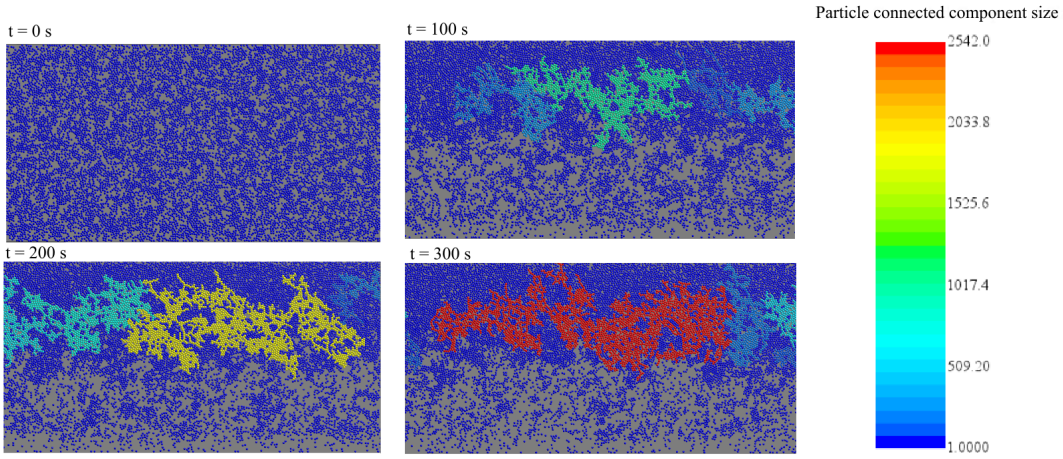

Figure 5.5: Maximum particle connected component size when the one-way coupling was selected in the model for case 1.

It can be shown that particles tend to accumulate at the upper part of the pipe, forming large chain-like agglomerates in a bed of hydrate particles. A transition from homogeneous to heterogeneous particle distribution occurs during the first 100 seconds. The largest agglomerate size was observed after 300 s according to the figure.

Fig. 5.6, shows the maximum agglomerate size at two different point in time after introducing the two-way coupling into the model. The figure shows a slightly reduced agglomerate size from the maximum after 300 s. This phenomenon is quite random due to the large flocculation in size with time.

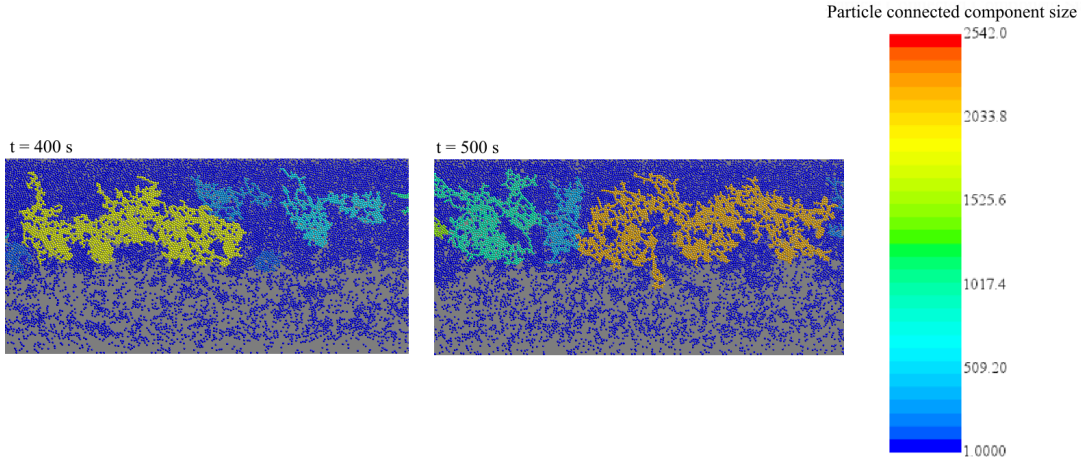

Figure 5.6: Maximum particle connected component size when the two-way coupling was selected in the model for case 1.

The distribution of particle connected component size as a function of the vertical direction of the pipe can be directly computed from STAR CCM+ and the results are shown in Fig. 5.7 (a). From this, the average connected component size can be calculated. Fig 5.7 (b) shows this parameter as a function of the vertical direction of the pipe. Two different points in time are shown: 300 s and 400 s.

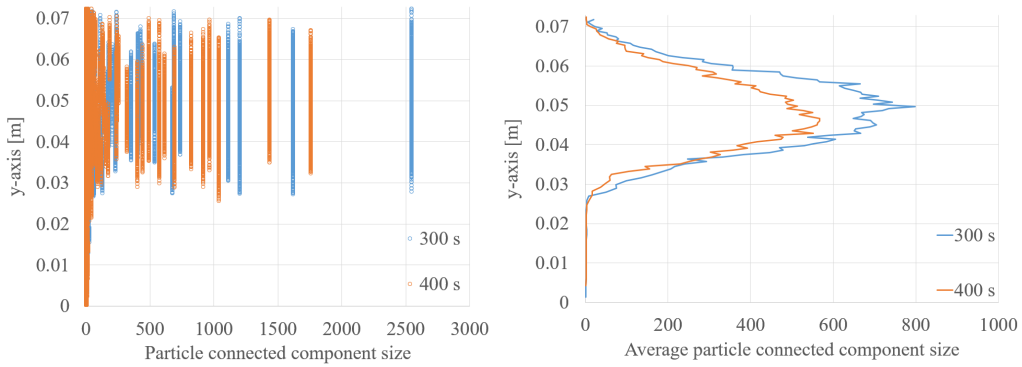

(a) **(b)**

Figure 5.7: Particle connected component size and the average particle connected component size as a function of the vertical y-direction of the pipe for case 1.

It can be shown from Fig. 5.7 (b) that the maximal average particle connected component size appears about 0.23 cm from the top wall, slightly above the middle of the pipe in the vertical direction. The maximal average number after 300 s was about 800 particles. At the time 400 s, the maximum average number was reduced to about 550 particles because the large agglomerate that appears after 300 s has been split into smaller agglomerates as shown in Fig 5.7 (a). Particles near the bottom wall contribute in the least degree to the agglomeration, followed by particles near the top wall.

Fig. 5.8 shows the volume and area fraction with respect to the vertical direction of the pipe right after particle injection, with the one-way coupled flow selected in the model, and after changing to the two-way coupled flow in the model. When introducing the two-way coupling in the model, it seems that particles become smoother distributed in the vertical direction, as shown in Fig. 5.8 (b). This may be because the particles affect the fluid and form a suspension referred to as a water-hydrate slurry. It is more difficult to see any trend from Fig. 5.8 (a).

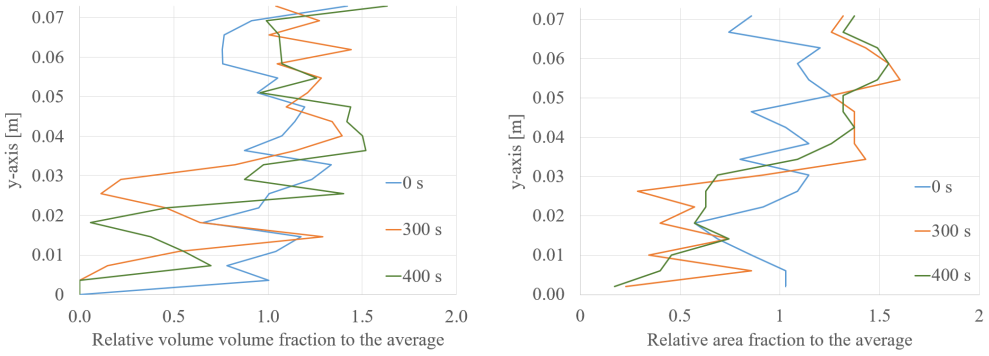

Figure 5.8: The relative volume fraction and area fraction of hydrate particles as a function of the vertical y-direction of the pipe for case 1.

The measurements were done 0.3 m from the pipe inlet. STAR CCM+ could measure the volume fraction, but was not able to measure the area fraction in a two-dimensional system. However, since the position of each particle can be found from simulations, a Fortran code was developed in this research to calculate the area fraction in the domain (see Appendix C). The domain was divided into a series of square cells, and the program calculated the area fraction in each cell. The number of cells in the vertical and horizontal direction, which defines the cell size affects the result (see Appendix D). The measurements that are shown in Fig. 5.8 (b) were based on 159 cells in the horizontal direction and 18 cells in the vertical direction of the pipe, corresponding to a cell size of $4{\cdot}10^{-3}$ m. This cell size was small enough to give good accuracy and large enough for all cells to contain particles so that the graph becomes relatively smooth and easy to interpret. The volume fraction calculated by STAR CCM+ gives greater

variations along the y-axis as shown in Fig. 5.8 (a). This indicate that the measurements are based on a relatively small cell size and the results and are more difficult to interpret.

Since particles are randomly injected into the domain, the relative area and volume fraction seems to be almost 1.0 along the vertical direction of the pipe right after injection. After 300 s of one-way coupled flow, substantially higher volume and area fraction were observed in the upper part of the pipe, than in the lower part. The high particle fraction part constitutes more than 50% of the vertical pipe direction, forming a bed of particles.

Fig. 5.9 shows the particle connected component size at five different times when the one-way coupling was selected in the model for case 2.

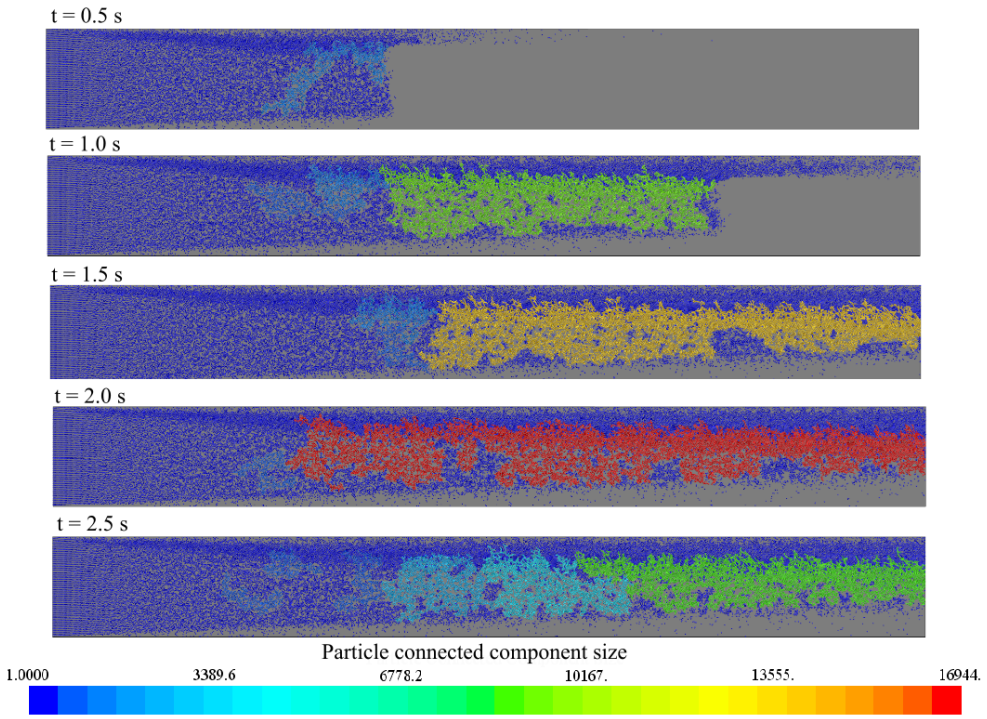

Figure 5.9: Maximum particle connected component size when the one-way coupling was selected in the model for case 2.

In case 2, a much larger maximum agglomerate was formed than in case 1. The main agglomerate was created centrally in the pipe vertical direction, and it moved as a part of the injected particle front as shown in Fig. 5.9. The agglomerate tended to be stable in the front, but not near the inlet surface, where the agglomerate was unstable, with agglomerate break-up and rebounding. The agglomerate size was the largest after 2 s, and splitting of the main agglomerate into two parts occurred at the time 2.5 s.

Fig. 5.10 shows the particle connected component size at two different points in time after changing to the two-way coupling in the model. When introducing the two-way coupling, there were no significant changes in the agglomerate size. The main agglomerate was divided into a smaller and a more substantial part. Due to significant fluctuations in the maximum size over time, the agglomerate size at a specific time was entirely random.

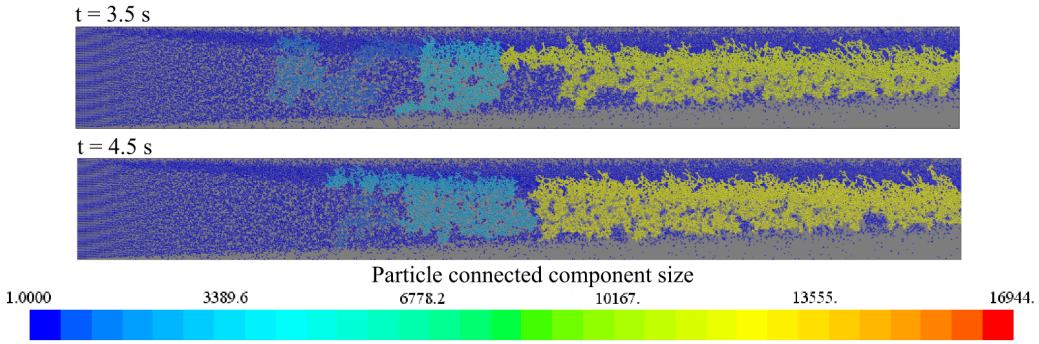

Figure 5.10: Maximum particle connected component size when the two-way coupling was selected in the model for case 2.

Fig. 5.11 (a) shows the distribution of particles in different particle connected component sizes and (b) the averaged size distribution. Two different points in time are shown: 2.5 s and 4.5 s.

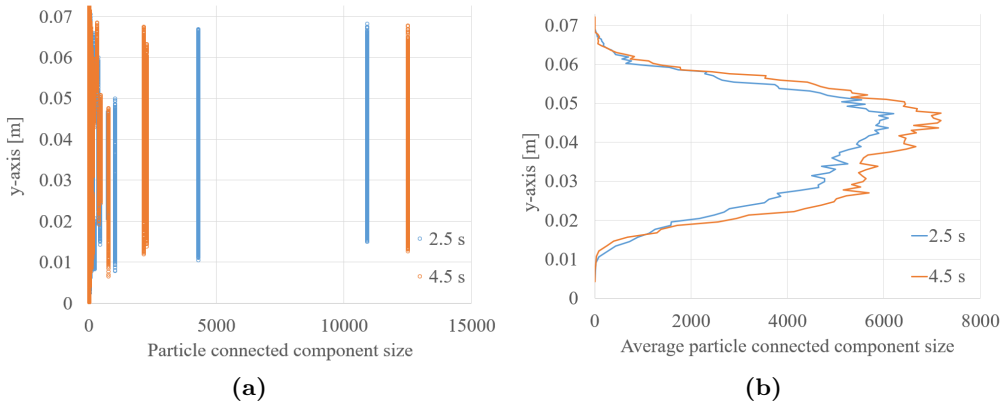

(a) **(b)**

Figure 5.11: Particle connected component size and the average particle connected component size as a function of the vertical y-direction of the pipe for case 2.

It can be shown from Fig 5.11 (b) that the maximal average particle connected component size appears at the distance about 0.25 cm from the top wall. This is slightly above the middle of the pipe in the vertical direction. After 2.5 s the maximum average number was about 6000 particles, and after 4.5 s about 6500 particles because the main agglomerate was slightly larger at this time. Similarly case 1, particles near the bottom wall contribute in the least degree to the agglomeration, followed by particles near the top wall.

Fig. 5.12 shows the relative volume and area fraction of hydrate particles as a function of the vertical y-direction in the pipe (0.3 m in the horizontal x-direction from the inlet) for case 2. The figure compares the results when the one-way coupling was selected, and after changing to the two-way coupling in the model. The volume and area fractions are found to be the lowest near the bottom of the pipe and the highest close to the top of the pipe. When introducing the two-way coupling, the variation with elevation becomes more smooth like found in case 1. As mentioned before, the concentration variation along the y-axis depends on the calculation method. The area fraction presented in Fig. 5.12 (b) was calculated based on a cell size of $4{\cdot}10^{-3}$ m. The influence of cell size when considering area fraction for case 2 is shown in Appendix D.

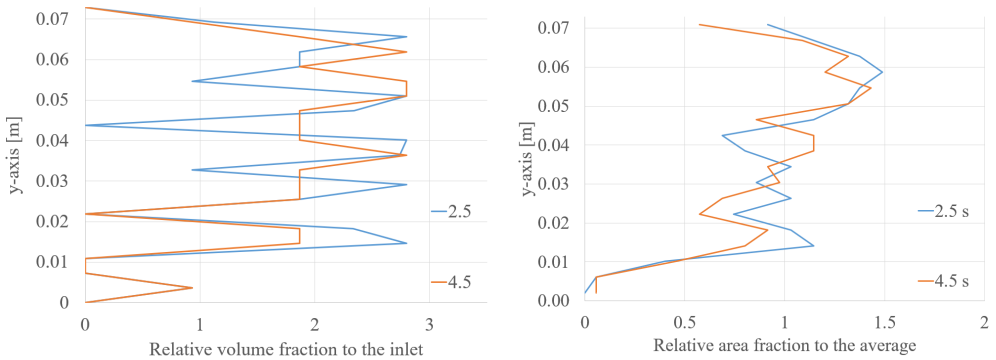

Figure 5.12: The relative volume fraction and area fraction of hydrate particles as function of the vertical y-direction for case 2.

The agglomerates are found to be chain-like clusters of particles, they are unstable and will split into several parts and grow along their way. As an illustration, Fig. 5.13 for case 1 and Fig. 5.14 for case 2 shows the particle connected component sizes at three consecutive time steps, of $\Delta T = 0.1$ s. The snapshot were taken at an arbitrary time equal to 200 s for case 1 and 2 s for case 2.

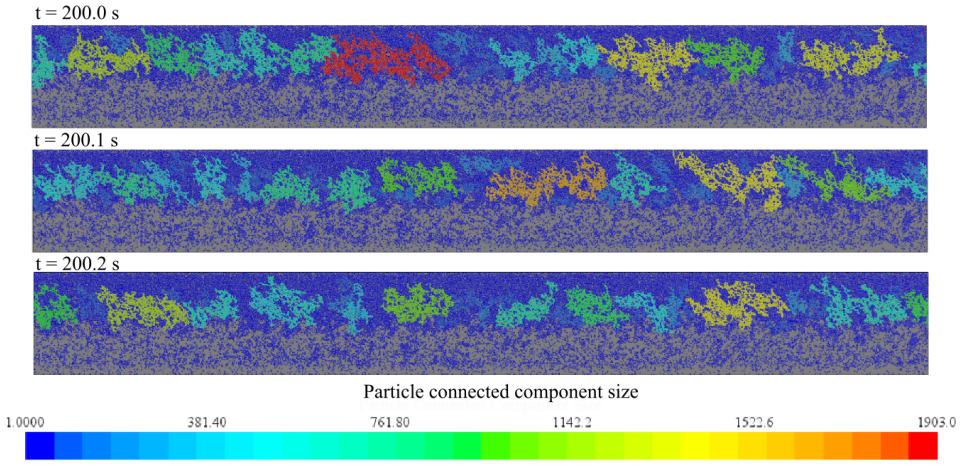

Figure 5.13: Illustration of flocculation in agglomeration size for case 1.

In case 1, the maximum particle agglomerate size varies from containing 1903 particles at t = 200.0 s to 1607 particles at t = 200.1 s and 14775 particles at t = 200.2 s. It seems that the change over time is most significant for the agglomerates consisting of the largest number of particles. They look most chain-like, and tend to divide into two or more parts over time, which significantly reduce their size.

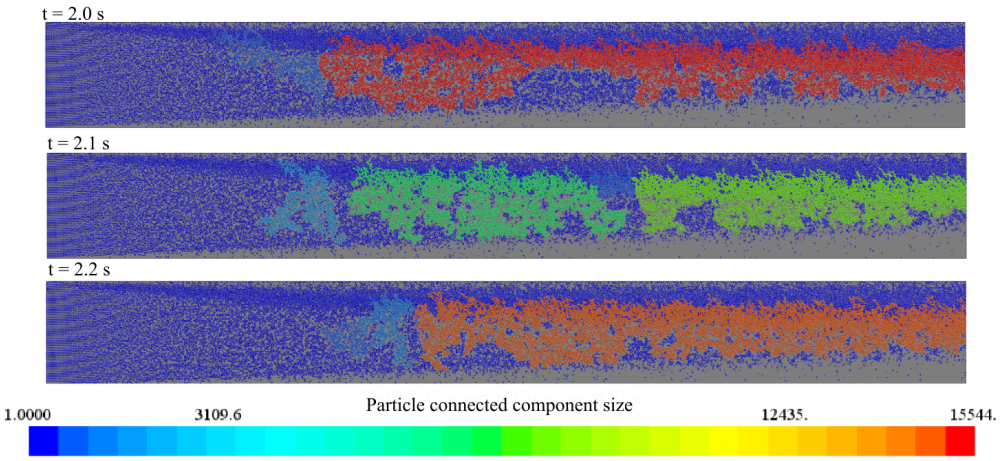

Figure 5.14: Illustration of flocculation in agglomeration size for case 2.

For case 2, as shown in Fig. 2.14, the maximum agglomerate size varies from containing 15544 particles at t = 2.0 s to 8559 particles at t = 2.1 s and 14775 particles at t = 2.2 s after starting particle injection.

5.3.2 Hydrate Deposition

Hydrate deposition means that particles connect to the wall. From the simulations, it can be shown that large deposits was not formed, but it would be interesting to see if any single particles deposited anyway.

The particle velocity distribution is almost the same for the fluid and the particles in the system. The momentum response time, which is the time required for a particle released from rest to achieve 63% of the free stream velocity was 0.02 s. This will allow the particles to achieve the carrier phase velocity relatively rapidly [25]. Hydrates will dissipate their kinetic energy in collisions with other particles and the pipeline wall, which slows down their motion. However, this reduction does not seem to be significant; hydrate particles obtain almost an identical velocity profile as the carrier fluid. When introducing the two-way coupling into the model, the particle velocity did not seen to change in the given time frame.

Fig 5.15 shows the particle velocity near the top and bottom wall when the one-way coupling and when the two-way coupling was selected in the model for case 1.

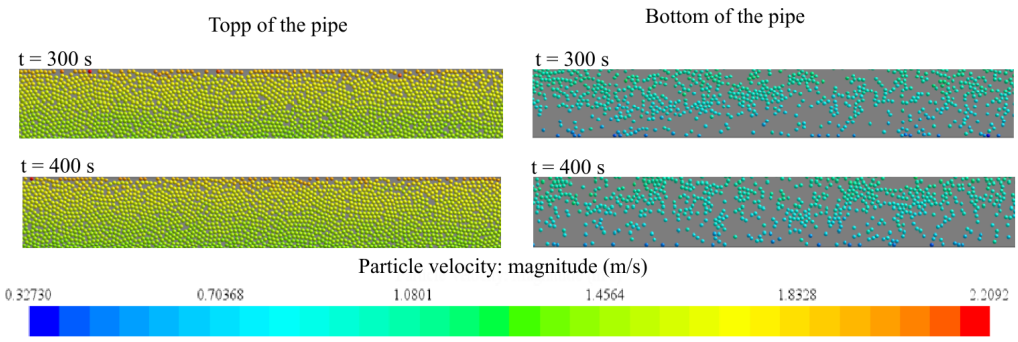

Figure 5.15: Particle velocity near the top and the bottom wall for case 1.

By taking a closer look at the particles near the top and bottom wall, it can be shown that single particles obtain the lowest velocity near the stationary bottom wall; they were then most likely to attach the wall. Single particles and rows of particles obtained the highest velocity near the top wall; they were then most likely to be captured by capillary effects.

For short time periods, the particle velocity was significantly reduced, which may indicate that they were about to stick to the wall. The minimum and maximum particle velocity can be used to study if particles deposit on the pipe wall. However, the lowest particle velocity shown in Fig. 5.16 (a) is about 0.05 m/s, which indicates that no particles deposit on the stationary bottom wall. The maximum particle velocity shown in Fig. 5.16 (b) is 2.44 m/s, and does

not reach the top wall velocity. The difference between the maximum particle velocity and the top wall is 0.03 m/s, which indicates that particles do not get captured by the wall.

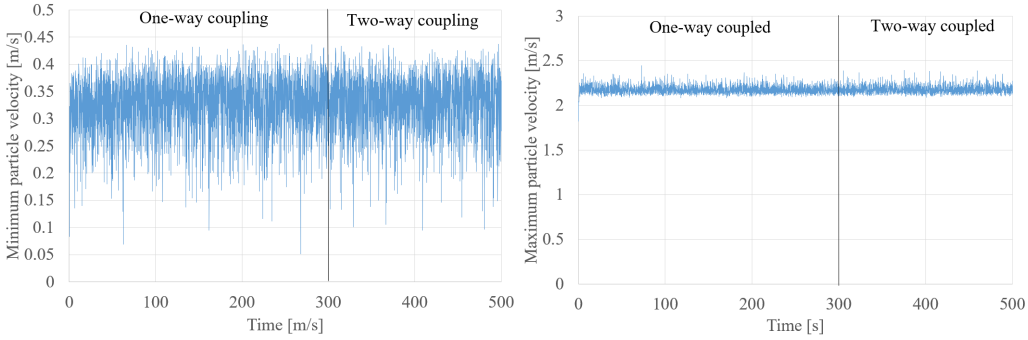

(a) Minimum particle velocity **(b)** Maximum particle velocity

Figure 5.16: Minimum and maximum particle velocity as a function of time for case 1.

Fig. 5.17 shows the particle velocity near the top and bottom wall when the one-way coupling and the two-way coupling was selected in the model for case 2.

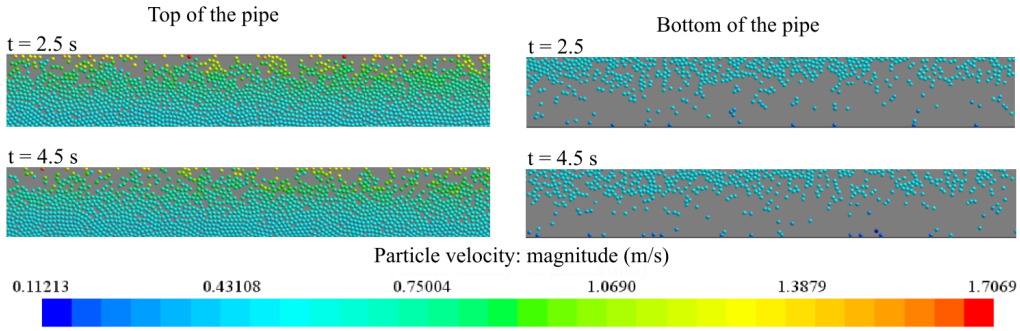

Figure 5.17: Particle velocity near the top and the bottom wall for case 2.

It can be shown from the figure that single particles obtain the highest velocity near the top wall and the lowest velocity near the bottom wall. The particle bed is much less densely packed near the top wall in this case, and not so many particles came in contact with the top wall.

The minimum and maximum particle velocity change during time for case 2, as shown in Fig. 5.18. The maximum particle velocity increases and the minimum particle velocity decreases during the 1.5 first seconds, and then becomes almost constant when the residence time of the particles in the simulated domain was reached. The lowest particle velocity obtained was 0 m/s and the highest velocity was 2.28 m/s. This indicates that a cluster of particles or more likely a

single particle connects to the bottom wall for a very short time. The difference between the top wall velocity and the maximum particle velocity is 0.19 m/s, and particles are then less closely to be captured at the top wall in this case than in case 1.

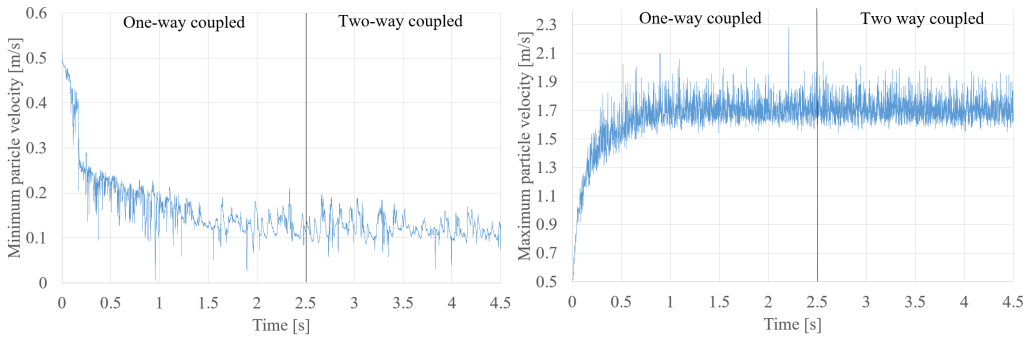

(a) Minimum particle velocity **(b)** Maximum particle velocity

Figure 5.18: Minimum and maximum particle velocity as a function of time for case 2.

5.4 Comparison with Other Works

Balakin et al. [4] assumed the CH_4 hydrate cohesion force to be seven times higher than the empirical relation for CyC5 model hydrates in gas. Fig. 5.19 shows that the empirical equation is in good accordance with the results from Nicolas et al. [47]. Results obtained for CH_4/C_2H_6 hydrates by Lee et al. are approximately seven times higher than the empirical equation for low subcooling values, $\Delta T \sim 3$, but the difference increases for higher subcooling values.

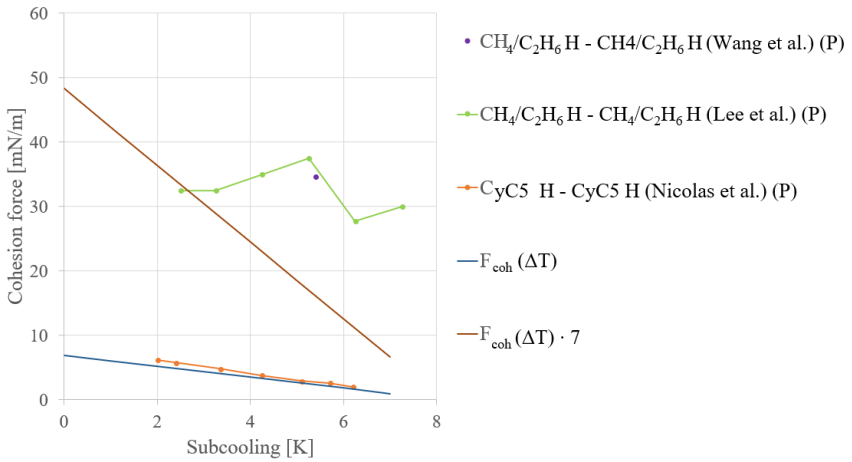

Figure 5.19: Work of cohesion for real and model hydrates.

From this research, the empirical formula based on force measurements using CyC5 model hydrates seems to differ quite a lot from the force calculated with real gas hydrates. A modification of the equation with a factor of 7 like done by Balakin et al. seems to be a good approximation for low subcooling values, but the deviation from real hydrate forces discussed in this thesis increases with subcooling.

From the experiment performed by Joshi et al. [5] plugging was attributed to the high resistance from the hydrate bed and wall deposits. It was not clear which mechanism is the most dominant for onset of hydrate plug formation: increased slurry viscosity or hydrate deposition on the pipe wall. The findings of this thesis indicate that large agglomerates do not connect to the pipeline steel bottom wall in the water phase. Only single particles and very small agglomerates obtained the lowest measured velocity near the wall, and afterwards were potentially attracted to the wall due to the hydrate adhesion force to steel. The shear force of the water-hydrate slurry seems to be sufficient to prevent hydrate deposition on the pipeline wall, like found by Lippmann et al. [56] and Aman et al. [6]. However, it should be mentioned that these simulations make use of an aggregated particle size (0.8 mm) from the primary particle size of ~ 8 μm [4], to limit the simulation time. This may be the reason for not observing any wall deposition of particles in the water phase at all. If the particle size is too high, the shear stress on the particles also becomes too high for deposition to occur. The examined particle size appears to exceed that limit, indicating that larger deposits are not able to deposit: this is only possible for smaller particles. However, deposition is found to be more likely to occur in the gas phase above by Aman et al. [6], which is a part of the the experimental pipe not considered in this thesis.

The other possible main mechanism of plugging, hydrate bed formation, was clearly observed according to the E-L simulations in this thesis. Large agglomerates showed to form, and a moving hydrate bed consisting of single particles and larger agglomerates was formed at the gas-slurry interphase after some time. The results found in these simulations are in good accordance with the results found by the E-E model performed by Balakin et al. [4]. They also observed high volume fraction of hydrate particles in the upper part of the pipe, constituting a hydrate bed and a very small volume fraction in the lower part of the pipe. Balakin et al. do not take into account the hydrate adhesive force to the wall material in their model, because the force was hard to estimate and could not be easily set in the E-E model. They then only investigate the effect of increased slyrry viscosity on the pressure. However, their results indicate that increased slurry viscosity results in about the same pressure drop profile with increased hydrate concentration in the water phase as found by the experiment performed by Joshi et al. [5].

Presence of hydrate particles in the water phase will form a slurry with properties that differ from those for just water. An example is viscosity that is higher due to fluid-particle interactions. The difference is most considerable in the upper part of the pipe with the highest particle concentration and the largest agglomerates. The formation of a week aggregated suspension is found in the literature to influence the flow in different ways. At high volume fractions, when hydrates connected into a network of particles, the suspension becomes solid-like [60], and the yield stress increases with particle volume fraction, ϕ_d. Significant yield stress can result in the formation of a hydrate plug and blockage of a pipeline [61]. The network of connected structures needs to be ruptured in order to make the material flowable. Therefore, hydrate slurries exhibit shear thinning behavior [61]. The viscosity decreases with shear velocity because shear forces become higher than the cohesive forces, the agglomerate size reduces, and the viscosity becomes more like that of water. In addition, hydrates may have a significant effect on the gas-liquid flow pattern in the flowline. The existence of gas hydrates and large agglomerates promotes a more chaotic flow pattern, and it is more difficult for gas-slurry systems to keep stable at stratified smooth flow [62, 63].

Hellestø et al. [35] discussed a potential threshold magnitude of the surface energy, $\sigma \in [0.00762, 0.04191]$ J/m^2, where stable cluster-cluster agglomeration no longer occurs. The surface energy used in this thesis was below this interval. Chain-like unstable agglomerates with extensive fluctuations in agglomerate size were found, which is supported by the results found by Hellestø et al.

Chapter 6

Conclusion

In this thesis, the Eulerian-Lagrangian DEM approach with the linear cohesion model was used for the numerical simulations. The hydrate-hydrate cohesion force and hydrate adhesion force to different wall materials have been discussed. The most relevant contact force options were converted into work by numerical simulations. The hydrate cohesion and adhesion work measured are important parameters influencing the process of hydrate agglomeration and deposition, and this issue was further numerically investigated for high water cut systems, using two models with different boundary conditions. This chapter presents the conclusions of the main findings of this thesis.

It was found possible to do a relatively good estimation of the work of cohesion in the model from CH_4/C_2H_6 hydrate-CH_4/C_2H_6 hydrate experimental cohesion force measurements performed by Wang et al. [53] and Lee et al. [2] using a high-pressure MMF apparatus. The work of cohesion between hydrate particles was estimated to be $W_{coh} = 6.968$ mJ/m^2. However, hydrate adhesion force to steel was not straightforward to find. The force was measured by Wang et al., but was found to be too low for the apparatus to detect. The best option was then to use calculations performed by Klyusov et al. [51] for CH_4 hydrates to steel using a less known force measurement apparatus. The work of adhesion was estimated to be $W_{adh} = 0.832$ mJ/m^2.

In this thesis, it was observed that the variation in hydrate forces with subcooling was not unambiguous. The results obtained by Klyusov et al. show that the hydrate adhesive force increased with subcooling. This was even more significant from the results achieved by Groisman et al. The opposite trend was observed by Nicolas et al. [47], which also is described in most of the literature works. The measurements by Groisman et al. were carried out at relatively high subcooling, and a possible explanation for this contradiction is that a minimum adhesive force exists. It is well known that the force reduces when the subcooling is increased. A minimum hydrate adhesive force could then explain results obtained by Groisman et al. [46] and Klyusov et al. [51].

Both simulations that studied the mechanism of hydrate plugging show significant agglomeration and no deposition in the water phase. Due to the different boundary conditions, the velocity profiles within the domain were different for the two cases. The mean velocity was found to be 1.23 m/s for case 1 and 0.54 m/s for case 2 in the middle of the pipe. Single particles experience the lowest velocity and were most likely to attach to the bottom wall. The shear force on the simulated particles seems to be too high for particle deposition to occur for both cases.

A large moving bed of hydrate particles that contained larger agglomerates was formed at the gas-slurry interphase over time. The agglomerate size increased during the time and stabilized at an equilibrium size, where the number of primary particles connected was about 2400 for case 1 and 14300 for case 2. Large fluctuations around this size were observed, and the largest agglomerate size observed for case 1 was about 7500 particles and for case 2 about 19000 particles. The maximum agglomerate size was then substantially higher for the case with the lowest average velocity, indicating that the shear velocity significantly affects the agglomerate size. The largest agglomerates were formed slightly above the middle of the pipe: about 0.23 cm from the top wall for case 1 and 0.25 cm for case 2. Agglomerates were found to be more chain-like and unstable with increased size.

According to these simulations, hydrate bed formation at the gas-slurry interphase seems to be an important mechanism for hydrate plug formation in high water cut systems, and from this research, probably the most dominating mechanism. Large agglomerates in the bed may contribute to form a highly viscous suspension with solid-like properties, which can result in pipeline plugging. Deposition in the water phase, on the other hand, does not appear to be the reason for pipeline plugging in such systems. However, potentially deposition in the gas phase above, not investigated in this thesis, may affect the plugging process. At the present time, the mechanism of pipeline plugging in high water cut systems is not fully understood.

Chapter 7

Future Work

This chapter discusses the identified opportunities and suggestions for further work.

Experimental investigation of gas hydrate forces for a large range of subcooling values will be necessary to determine if there exists a minimum contact force in this interval of subcooling values. Attention should be paid to the rang starting at a very low value, $\Delta T \sim 0$ K, to a relatively high value, $\Delta T \sim 20$. If a minimum is found for adhesion/cohesion force, this will be important information in the effort to prevent hydrate deposition/agglomeration in pipelines.

Experimental force measurements are mainly performed in a gas phase in literature. To get a more accurate estimate of the hydrate interaction forces in the water phase, experiments in this phase are required. Generally, there exists limited literature research about hydrated adhesion forces to various surface materials, and further investigation in this area is needed to get a more accurate picture of possible deposition in pipeline systems.

Setting up the simulations with the appropriate physical models is the key to obtain accurate results. However, adding models for physical influences, increases the computational cost. Therefore, a balance must be found between the two priorities. For this reason, the most time-consuming simulations with a large number of particles were simplified to a two-dimensional system in this research. The resulting data would, therefore, differ some from the real three-dimensional systems. It is not known to which extent this affected the quality of the results. For further work, it could therefore be interesting to simulate the three-dimensional system. To run such a simulation, a supercomputer with great capacity is recommended.

Gas hydrate agglomeration and deposition simulations were in this thesis limited to elongated pipes without angles. The experimental flowloop that was studied by Joshi et al. [5] contained elbows. For further work, it could, therefore, be interesting to study hydrate agglomeration and deposition in a pipe with a complex geometry.

Appendices

Appendix A

Material Properties

This thesis focus on CH_4 hydrate and carbon steel as the surface material. Other hydrate formers and surface materials are discussed in the thesis, but not examined by simulations. This Appendix gives the material properties for all hydrate and surface materials discussed.

Wall Material Properties

Table A.1: Wall material properties.

Wall Material	Material properties	Value	Unit
Steel	Density, ρ	7837	$\frac{\text{kg}}{\text{m}^3}$
	Poisson Ratio, ν	0.285	-
	Youngs modulus, E	$2.0 \cdot 10^{11}$	Pa
Aluminium alloy	Density, ρ	280	$\frac{\text{kg}}{\text{m}^3}$
	Poisson Ratio, ν	0.33	-
	Youngs modulus, E	$7.24 \cdot 10^{10}$	Pa
Fluoroplastic	Density, ρ	2151	$\frac{\text{kg}}{\text{m}^3}$
	Poisson Ratio, ν	0.46	-
	Youngs modulus, E	$1.53 \cdot 10^{9}$	Pa
Mica	Density, ρ	2950	$\frac{\text{kg}}{\text{m}^3}$
	Poisson Ratio, ν	0.25	-
	Youngs modulus, E	$7.07 \cdot 10^{10}$	Pa
Calcite	Density, ρ	2710	$\frac{\text{kg}}{\text{m}^3}$
	Poisson Ratio, ν	0.30	-
	Youngs modulus, E	$7.50 \cdot 10^{10}$	Pa
Copper	Density, ρ	8940	$\frac{\text{kg}}{\text{m}^3}$
	Poisson Ratio, ν	0.35	-
	Youngs modulus, E	$1.1 \cdot 10^{11}$	Pa

In STAR CCM+, it is possible to chose wall material in the program, this list do not contain chose for fluoroplastic, mica and calsite. Material properties for this materials has to be found from literature: [64, 65]

Surface Energy

Table A.2: Table of surface energy values of solid materials. Adapted from Kingloch, Santhanaml et al. and Israelachvili [66, 67, 29].

Material Type	Surface energy, σ $[\frac{\text{mN}}{\text{m}}]$
Low energy surfaces - plastic, rubber and composites	
Polyhexafluoropropylene	12.4
Polytetrafluoroetylene - PTFE	19.1
Poly(vinylidene fluoride) - PVF	30.3
Poly(chlorotrifluoroethylene)	33.5
High Energy Surfaces - metals, oxides and ceramics	
Aluminium	800
Copper	1600
Mica	120
Calcite	230
Ice	110

Hydrate Density

Table A.3: Tabel of hydrate density.

Hydrate former	Density, ρ_d $[\frac{\text{kg}}{\text{m}^3}]$
CH_4	910.0
CH_4/C_2H_6	940.0
CO_2	1115.0
THF	997.0
F-12/natural gas	976.1
Normal ice	916.7
CyC5	940.0

Various formers result in different values of hydrate density. Density of CO_2, CH_4, THF and CyC_5 hydrates can easily be found [68, 69, 5, 70, 14], while the density of F-12/natural gas mixture hydrate has to be calculated. Density of F-12 hydrate is found to be 1130 kg/m^3 accordance to Mori et al. [71] and density of natural gas hydrate consisting mainly of CH_4 hydrate former is estimated to

be 910 kg/m^3. A result is an SII hydrate, where F-12 will fill the large cavities and natural gas will fill the small cavities. SII hydrates consist of 8 large cavities and 16 small cavities (see Fig. 2.2), and this results in a composition of 33% F-12 and 66 % natural gas, so that the hydrate density becomes 976.1 kg/m^3.

Friction Coefficients between Ice and Different Wall Materials

Table A.4: Static friction coefficients between ice and different wall materials adapted from Bowden and Sukhorukov et al. [72, 73].

Surface material	Static friction coefficient [-]
Steel	0.46
Duralumin	0.30
Fluoroplastic	0.06
Copper	0.50
Ice	0.62

Appendix B

Conversion of Forces

This Appendix presents conversion of experimental hydrate forces to the force for the simulated system shown in Fig. 4.1.

Table B.1: CH_4/C_2H_6 hydrate-CH_4/C_2H_6 hydrate cohesion force (hydrate particle diameter $\sim$ 500 μm) from Lee et al. [2].

Material	F_{ss} [N]$\cdot 10^6$	A_H [J]$\cdot 10^{19}$	F_{sp} [N]$\cdot 10^5$	$\frac{F_{sp}}{D}$ [$\frac{\mathrm{N}}{\mathrm{m}}$]$\cdot 10^2$	ΔT [K]
H-H	8.12	4.93	2.60	3.25	2.50
H-H	8.12	4.93	2.60	3.25	3.25
H-H	8.75	5.31	2.80	3.50	4.25
H-H	9.37	5.68	3.00	3.75	5.25
H-H	6.94	4.21	2.22	2.77	6.25
H-H	7.50	4.55	2.40	3.00	7.25

Table B.2: CH_4/C_2H_6 hydrate-CH_4/C_2H_6 hydrate cohesion force and CH_4/C_2H_6 hydrate-CS adhesion force (hydrate particle diameter $\sim$ 800 μm) from Wang et al. [53].

Material	F_{ss} or F_{sp} [N]$\cdot 10^6$	A_H [J]$\cdot 10^{19}$	F_{sp} [N]$\cdot 10^5$	$\frac{F_{sp}}{D}$ [$\frac{\mathrm{N}}{\mathrm{m}}$]$\cdot 10^2$	ΔT [K]
H-H	13.88	5.26	2.78	3.47	5.40
H-CS**	1.36	0.26	0.14	0.17	5.40

Table B.3: Hydrate adhesion/cohesion force (hydrate cylinder of diameter $\sim$ 6.7 mm) from Jung et al. [45].

Material	F_{pp} [N]	A_H [J]$\cdot 10^{21}$	F_{sp} [N]$\cdot 10^7$	$\frac{F_{sp}}{D}$ $[\frac{\text{N}}{\text{m}}]\cdot 10^4$	ΔT [K]
CH_4 H-CH_4 H	6.35	4.82	2.54	3.18	9.38
CO_2 H-CO_2 H	6.22	4.72	2.49	3.12	6.19
THF H-Calcite	5.69	4.32	2.28	2.85	4.40
CH_4 H-Mica	3.74	2.84	1.50	1.87	9.38
CO_2 H-Mica	4.46	3.39	1.79	2.23	6.19
THF H-Mica	4.64	3.52	1.86	2.32	4.40

Table B.4: CH_4 hydrate-CS adhesion force (CS cylinder diameter 20 mm and hight 10 mm) from Klyusov et al. [51]. The asterisk, * indicates that the surface is polished.

Material	F_{pp} [N]	A_H [J]$\cdot 10^{22}$	F_{sp} [N]$\cdot 10^9$	$\frac{F_{sp}}{D}$ $[\frac{\text{N}}{\text{m}}]\cdot 10^4$	ΔT [K]
H-CS*	2.90	1.24	6.53	7.45	4.85
H-CS*	3.00	1.28	6.74	7.75	5.35
H-CS	3.40	1.45	7.64	8.75	5.90
H-CS	4.00	1.70	9.00	9.35	6.58

Table B.5: CyC5 hydrate-CyC5 hydrate cohesion force and CyC5 hydrate-CSadhesion force ((hydrate particle diameter $\sim$ 30 μm) from Nicolas et al. [47]

Material	F_{ss} or F_{sp}[N]$\cdot 10^8$	A_H [J]$\cdot 10^{20}$	F_{sp} [N]$\cdot 10^6$	$\frac{F_{sp}}{D}$ $[\frac{\text{N}}{\text{m}}]\cdot 10^3$	ΔT [K]
H-H	9.30	9.39	4.96	6.20	2.00
H-H	8.70	8.79	4.64	5.80	2.40
H-H	7.20	7.28	3.84	4.80	3.35
H-H	5.70	5.76	3.04	3.80	4.24
H-H	4.35	4.40	2.32	2.90	5.10
H-H	3.90	3.94	2.08	2.60	5.70
H-H	3.00	3.03	1.60	2.00	6.20
H-CS	2.48	1.25	0.66	0.82	0.40
H-CS	3.75	0.19	0.10	0.12	3.65

Table B.6: Hydrate-CS surface adhesive force (hydrate cylinder diameter $\sim$ 30 mm) from Groisman et al. [46].

Material	F_{pp} [N]	A_H [J]$\cdot 10^{20}$	F_{sp} [N]$\cdot 10^7$	$\frac{F_{sp}}{D}$ $[\frac{\mathrm{N}}{\mathrm{m}}]\cdot 10^4$	ΔT [K]
Shear experiments					
F-12/CH_4 H-CS	49.48	0.19	0.99	1.24	3.95
F-12/CH_4 H-CS	63.62	0.24	1.27	1.59	5.95
F-12/CH_4 H-CS	155.51	0.59	3.11	3.88	8.55
F-12/CH_4 H-CS	784.61	2.97	15.68	19.60	18.95
THF H-CS	162.58	0.62	3.25	4.06	5.95
THF H-CS	303.49	1.15	6.07	7.59	7.95
THF H-CS	501.87	1.90	10.03	12.54	12.15
THF H-CS	614.97	2.33	12.29	15.36	16.35
THF H-CS	650.31	2.46	12.99	16.24	20.65
Pull-off experiments					
THF H-CS	91.89	0.11	1.84	2.29	3.35
THF H-CS	233.26	0.88	4.66	5.83	4.45
THF H-CS	282.74	3.48	5.65	7.06	8.45

Table B.7: Hydrate-duralumin (Al) surface adhesive force (hydrate cylinder diameter $\sim$ 30 mm) from Groisman et al. [46].

Material	F_{pp} [N]	A_H [J]$\cdot 10^{21}$	F_{sp} [N]$\cdot 10^7$	$\frac{F_{sp}}{D}$ $[\frac{\mathrm{N}}{\mathrm{m}}]\cdot 10^4$	ΔT [K]
Shear experiments					
F-12/CH_4 H-Al	56.55	2.14	1.13	1.41	2.65
F-12/CH_4 H-Al	56.05	2.14	1.13	1.41	6.05
F-12/CH_4 H-Al	63.62	2.41	1.27	1.59	7.05
F-12/CH_4 H-Al	98.96	3.75	1.98	2.47	8.05
F-12/CH_4 H-Al	106.03	4.01	2.12	2.65	9.75
F-12/CH_4 H-Al	134.30	5.09	2.86	3.58	12.15
Pull-off experiments					
THF H-Al	91.89	3.480	1.84	2.29	6.15
THF H-Al	98.96	3.747	1.98	2.47	7.85
THF H-Al	219.13	8.298	4.38	5.47	9.75
THF H-Al	261.54	9.904	5.23	6.53	12.35
THF H-Al	346.36	13.12	6.92	8.65	15.65
THF H-Al	409.98	15.52	8.19	10.24	17.35
F-12/CH_4 H-Al	77.75	2.94	1.55	1.94	8.05
F-12/CH_4 H-Al	106.03	4.01	2.12	2.65	10.45
F-12/CH_4 H-Al	143.30	5.09	2.68	3.35	13.05

Table B.8: Hydrate-fluoroplastic (Fl) surface adhesive force (hydrate cylinder diameter $\sim$ 30 mm) from Groisman et al. [46].

Material	F_{pp} [N]	A_H [J]$\cdot 10^{21}$	F_{sp} [N]$\cdot 10^7$	$\frac{F_{sp}}{D}$ $[\frac{\mathrm{N}}{\mathrm{m}}]\cdot 10^4$	ΔT [K]
Shear experiments					
THF H-Fl	49.48	1.87	0.99	1.24	1.45
THF H-Fl	63.62	2.41	1.27	1.59	4.45
THF H-Fl	70.69	2.68	1.41	1.77	8.65
THF H-Fl	70.69	2.68	1.41	1.77	11.45
F-12/CH_4 H-Fl	49.48	1.87	0.99	1.24	3.75
F-12/CH_4 H-Fl	56.55	2.14	1.12	1.40	6.55
F-12/CH_4 H-Fl	63.62	2.41	1.27	1.59	9.35
F-12/CH_4 H-Fl	63.62	2.41	1.27	1.59	15.75
Pull-off experiments					
THF H-Fl	31.102	1.18	0.62	0.78	3.95
THF H-Fl	56.549	2.14	1.12	1.40	8.15
THF H-Fl	70.686	2.68	1.41	1.77	10.15
THF H-Fl	70.686	2.68	1.41	1.77	12.25
THF H-Fl	70.686	2.68	1.41	1.77	15.25
THF H-Fl	74.220	2.81	1.48	1.85	19.45
F-12/CH_4 H-Fl	30.39	1.15	0.61	0.76	4.05
F-12/CH_4 H-Fl	70.69	2.68	1.41	1.77	7.05
F-12/CH_4 H-Fl	84.82	3.21	1.69	2.12	14.55
F-12/CH_4 H-Fl	70.69	2.68	1.41	1.77	17.55
F-12/CH_4 H-Fl	70.69	2.68	1.41	1.77	19.55

Appendix C

Fortran Code

This Appendix presents the program for measuring area fraction of hydrate particles in each cell constituting the domain. The position of each particle comes from STAR CCM+, stored in a file called "simulation.txt" and information about the domain size, particle size and number of cells are stored in a file called data.txt. The program was compiled with Fortran 77.

```
----------DECLARATION----------

      IMPLICIT NONE

      REAL xp(1000000), yp(1000000)
      REAL aL, aH, aD, pi
      INTEGER i, j, k, N, M, nPar
      REAL dx, dy, areafrac
      pi = 3.141592654

C     N: Number of cells along x
C     M: Number of cells along y
C     nPar: Number of particles

C     xp(1000000): Particle position in x-direction
C     yp(1000000): Particles position in y-direction

C     aL: Length of the domain [m]
C     aH: Height of the domain [m]
C     aD: Particle diameter [m]

C     dx: Length of each cell [m]
C     dy: Hight of each cell [m]
C     areafrac: Area fraction
```

```
———————— THE CODE STARTS WITH OPENING FILES ————————

      open(1,file='simulation.txt')
      open(2,file='data.txt')
      open(3,file='areafrac.txt')

————————————READING FROM THE simulation.txt FILE————————————

      count=0
      i=0
1     i=i+1
      read(1,*,end=99)xp(i),yp(i)
      go to 1
99    continue !the whole file has been read - the code finishes


      count=i-1
      write(*,*) 'There are ',count,'particles in the system'
      close(1)

————————————————————READING data.txt————————————————————

      read(2,*)aL
      read(2,*)aH
      read(2,*)aD
      read(2,*)N
      read(2,*)M
      close(2)

      dx=aL/N
      dy=aH/M

      write(*,*)'size step', dx,dy

————————————————————CALCULATE AREA FRACTION————————————————————

      do  i=1,N
      do  j=1, M

      nPar=0
      do  k=1,count
      if(xp(k).le.i*dx.and.xp(k).gt.(i-1)*dx.and.
&yp(k).le.j*dy.and.yp(k).gt.(j-1)*dy)nPar=nPar+1
      end do
```

```
areafrac=nPar*pi*aD*aD/4/(dx*dy)*100
write(3,*)0.5*(i*dx+(i-1)*dx),0.5*(j*dy+(j-1)*dy),areafrac

end do
end do

close(3)

end
```

Appendix D

Importance of Cell Size in the Fortran Code

The resulting area fraction as function of the vertical y-direction of the pipe depends on the cell size. A smaller cell size gives more accuracy. However, if the cell size is too small, it will cause some cells to be free of particles. This will lead to very large variations, and the trend from the results could be unclear.

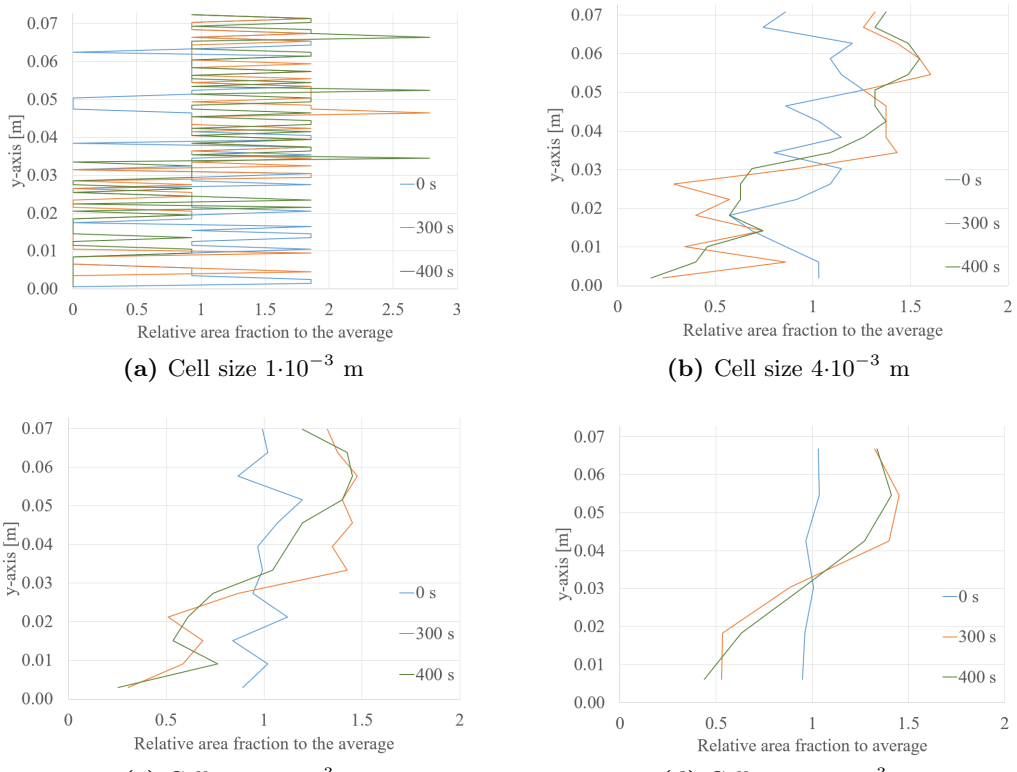

(a) Cell size $1{\cdot}10^{-3}$ m

(b) Cell size $4{\cdot}10^{-3}$ m

(c) Cell size $6{\cdot}10^{-3}$ m

(d) Cell size $12{\cdot}10^{-3}$ m

Figure D.1: Comparison of area fraction calculated based on different cell sizes for case 1.

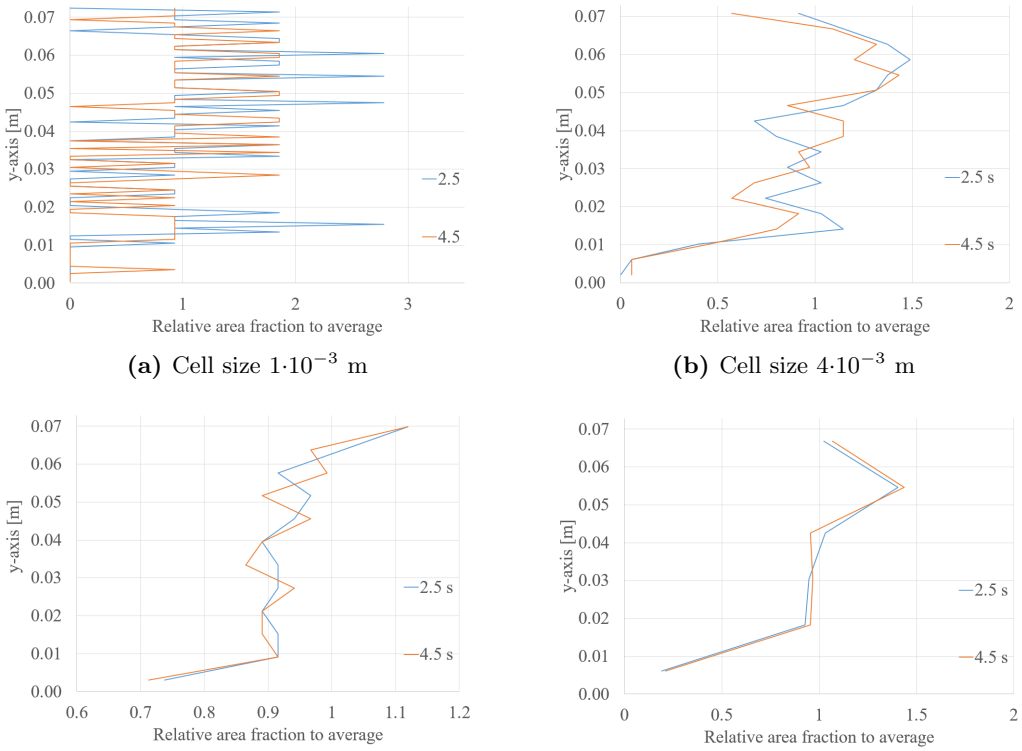

(a) Cell size $1{\cdot}10^{-3}$ m

(b) Cell size $4{\cdot}10^{-3}$ m

(c) Cell size $6{\cdot}10^{-3}$ m

(d) Cell size $12{\cdot}10^{-3}$ m

Figure D.2: Comparison of area fraction calculated based on different cell sizes for case 2.

The area fractions presented in Fig. D.1 and D.2 (a) and (b) and (d) are measured 0.30 m in x-direction from the pipe inlet, and the area fraction shown in (c) is measured 0.33 m in x-direction from the pipe inlet.

Bibliography

[1] EG Hammerschmidt. Formation of gas hydrates in natural gas transmission lines. *Industrial & Engineering Chemistry*, 26(8):851–855, 1934.

[2] Bo Ram Lee and Amadeu K Sum. Micromechanical cohesion force between gas hydrate particles measured under high pressure and low temperature conditions. *Langmuir*, 31(13):3884–3888, 2015.

[3] Robert E Cohen Subramanian, Gareth H McKinley, and Kripa K Varanasi. Hydrate-phobic surfaces: Fundamental studies in clathrate hydrate adhesion reduction.

[4] BV Balakin, A Kosinska, and KV Kutsenko. Pressure drop in hydrate slurries: rheology, granulometry and high water cut. submitted.

[5] Sanjeev V Joshi, Giovanny A Grasso, Patrick G Lafond, Ishan Rao, Eric Webb, Luis E Zerpa, E Dendy Sloan, Carolyn A Koh, and Amadeu K Sum. Experimental flowloop investigations of gas hydrate formation in high water cut systems. *Chemical Engineering Science*, 97:198–209, 2013.

[6] Zachary M Aman, Hao Qin, Marshall Pickarts, Mauricio Di Lorenzo, Eric F May, Carolyn A Koh, Luis E Zerpa, et al. Deposition and shear stress initial investigations for hydrate blockage. In *Offshore Technology Conference*. Offshore Technology Conference, 2018.

[7] Shlumberger. The promise of an untapped energy source, 2010.

[8] John Carroll. *Natural gas hydrates: a guide for engineers*. Gulf Professional Publishing, 2014.

[9] Jorge F Gabitto and Costas Tsouris. Physical properties of gas hydrates: A review. *Journal of Thermodynamics*, 2010, 2010.

[10] E Dendy Sloan Jr. Fundamental principles and applications of natural gas hydrates. *Nature*, 426(6964):353, 2003.

[11] Keith C Hester and Peter G Brewer. Clathrate hydrates in nature. *Annual review of marine science*, 1:303–327, 2009.

[12] E Dendy Sloan. Gas hydrates: Review of physical/chemical properties. *Energy & Fuels*, 12(2):191–196, 1998.

[13] Boris V Balakin. Experimental and theoretical study of the flow, aggregation and deposition of gas hydrate particles. 2010.

[14] E Dendy Sloan Jr and Carolyn Koh. *Clathrate hydrates of natural gases*. CRC press, 2007.

[15] Bjørn Kvamme. Fundamentals of natural gas hydrates and practical implications. University of Bergen, (PTEK232), 2017.

[16] Luis E Zerpa, E Dendy Sloan, Amadeu K Sum, and Carolyn A Koh. Overview of csmhyk: A transient hydrate formation model. *Journal of Petroleum Science and Engineering*, 98:122–129, 2012.

[17] Masoumeh Akhfash, Zachary M Aman, Sang Yoon Ahn, Michael L Johns, and Eric F May. Gas hydrate plug formation in partially-dispersed water–oil systems. *Chemical Engineering Science*, 140:337–347, 2016.

[18] Simon Davies, John Boxall, Laura Dieker, Amadeu Sum, Carolyn Koh, E Dendy Sloan, Jefferson Louis Creek, Zheng-Gang Xu, et al. Improved predictions of hydrate plug formation in oil-dominated flowlines. In *Offshore Technology Conference*. Offshore Technology Conference, 2009.

[19] Joseph W Nicholas, Ryan R Inman, John PH Steele, Carolyn A Koh, and E Dendy Sloan. A modelling approach to hydrate wall growth and sloughing in a water saturated gas pipeline. In *Proceedings of the 6th International Conference on Gas Hydrates (ICGH 2008)*, pages 6–10, 2008.

[20] Ahmad AA Majid, Giovanny Grasso, Jefferson L Creek, Hao Qin, Thomas Charlton, Douglas Estanga, Mayela Rivero, Ben Bbosa, Amaka Waturuocha, Mike Volk, et al. A review of hydrate formation for partially dispersed systems in multiphase flow conditions and the detection of hydrate deposits. In *Offshore Technology Conference*. Offshore Technology Conference, 2017.

[21] Jefferson Louis Creek, Sivakumar Subramanian, Douglas Alexander Estanga, et al. New method for managing hydrates in deepwater tiebacks. In *Offshore Technology Conference*. Offshore Technology Conference, 2011.

[22] Emilie Colombel, Patrick Gateau, Loïc Barré, Frédéric Gruy, and Thierry Palermo. Discussion of agglomeration mechanisms between hydrate particles in water in oil emulsions. *Oil & Gas Science and Technology-Revue de l'IFP*, 64(5):629–636, 2009.

[23] Malcolm A Kelland. History of the development of low dosage hydrate inhibitors. *Energy & fuels*, 20(3):825–847, 2006.

[24] John C Berg. *An introduction to interfaces & colloids: the bridge to nanoscience*. World Scientific, 2010.

[25] Clayton T Crowe, John D Schwarzkopf, Martin Sommerfeld, and Yutaka Tsuji. *Multiphase flows with droplets and particles*. CRC press, 2011.

[26] Aslak Hellestø. A study of orthokinetic agglomeration in cohesive multiphase flows. Master's thesis, The University of Bergen, 11 2015.

[27] Shuji Himeno, Toshihiro Tomita, Kenji Suzuki, and Shuichi Yoshida. Characterization and selectivity for methane and carbon dioxide adsorption on the all-silica dd3r zeolite. *Microporous and Mesoporous Materials*, 98(1):62–69, 2007.

[28] Dimo Kashchiev and Abbas Firoozabadi. Nucleation of gas hydrates. *Journal of crystal growth*, 243(3-4):476–489, 2002.

[29] Jacob N Israelachvili. *Intermolecular and surface forces*. Academic press, 2011.

[30] Shuiqing Li, Jeffrey S Marshall, Guanqing Liu, and Qiang Yao. Adhesive particulate flow: The discrete-element method and its application in energy and environmental engineering. *Progress in Energy and Combustion Science*, 37(6):633–668, 2011.

[31] Jr. Anderson, John David. *Computational Fluid Dynamics: The Basic with application*. Mc Graw Hill Education, 1995.

[32] D John and JR Anderson. Computational fluid dynamics: the basics with applications. *P. Perback, International ed., Published*, 1995.

[33] StarCCM+. *Star CCM+, User guide for version 12.02*, 2017.

[34] Jeffery S Marshall and Shuiqing Li. *Adhesive particle flow*. Cambridge University Press, 2014.

[35] Aslak S Hellestø, Maryam Ghaffari, Boris V Balakin, and Alex C Hoffmann. A parametric study of cohesive particle agglomeration in a shear flow—numerical simulations by the discrete element method. *Journal of Dispersion Science and Technology*, 38(5):611–620, 2017.

[36] Rahul Garg, Janine Galvin, Tingwen Li, and Sreekanth Pannala. Documentation of open-source mfix–dem software for gas-solids flows. *From URL https://mfix. netl. doe. gov/documentation/dem_doc_2012-1. pdf.(Accessed: 31 March 2014)*, 2010.

[37] KL Johnson and K Johnson. Normal contact of elastic solids: Hertz theory. *Contact mechanics*, pages 84–106, 1985.

[38] Xiaoyin Zhu. Tutorial on hertz contact stress. In *Opti*, volume 521, pages 1–8, 2012.

[39] RD Mindlin. Compliance of elastic bodies in contact. *J. Appl. Mech. Trans. ASME*, 16:259–268, 1949.

[40] Pawel Kosinski and Alex C Hoffmann. Extension of the hard-sphere particle-wall collision model to account for particle deposition. *Physical review E*, 79(6):061302, 2009.

[41] Pawel Kosinski and Alex C Hoffmann. An extension of the hard-sphere particle–particle collision model to study agglomeration. *Chemical Engineering Science*, 65(10):3231–3239, 2010.

[42] Pawel Kosinski and Alex C Hoffmann. Extended hard-sphere model and collisions of cohesive particles. *Physical Review E*, 84(3):031303, 2011.

[43] Warren L McCabe, Julian C Smith, and Peter Harriott. *Unit operations of chemical engineering*, volume 4. McGraw-Hill New York, 1985.

[44] Fan Jin, Xu Guo, and Huajian Gao. Adhesive contact on power-law graded elastic solids: the jkr–dmt transition using a double-hertz model. *Journal of the Mechanics and Physics of Solids*, 61(12):2473–2492, 2013.

[45] JW Jung and J Carlos Santamarina. Hydrate adhesive and tensile strengths. 2011.

[46] A.G Groisman and A.Z Savvin. Adhesive properties of gas hydrates. *Natural and technological gas hydrates*, 1990. [in Russian].

[47] Joseph W Nicholas, Laura E Dieker, E Dendy Sloan, and Carolyn A Koh. Assessing the feasibility of hydrate deposition on pipeline walls—adhesion force measurements of clathrate hydrate particles on carbon steel. *Journal of Colloid and Interface Science*, 331(2):322–328, 2009.

[48] Sung-oh Yang, Derek M Kleehammer, Zhongxin Huo, E Dendy Sloan, and Kelly T Miller. Temperature dependence of particle–particle adherence forces in ice and clathrate hydrates. *Journal of colloid and interface science*, 277(2):335–341, 2004.

[49] Laura E Dieker, Craig J Taylor, Carolyn A Koh, and E Dendy Sloan. Micromechanical adhesion force measurements between cyclopentane hydrate particles. In *Proceedings of the 6th International Conference on Gas Hydrates*, pages 12–16. Citeseer, 2008.

[50] Craig J Taylor, Laura E Dieker, Kelly T Miller, Carolyn A Koh, and E Dendy Sloan. Micromechanical adhesion force measurements between tetrahydrofuran hydrate particles. *Journal of Colloid and Interface Science*, 306(2):255–261, 2007.

[51] V.A Klyusov and L.M Gukhman. Study of adhesive capacity of gas hydrates to metal surface. *Ministry of gas industry*, 1975. [in Russian].

[52] BV Balakin, MI Delov, A Kosinska, KV Kutsenko, and AA Lavrukhin. Heat transfer during transition to nucleate boiling. *International Journal of Heat and Mass Transfer*, 91:1101–1105, 2015.

[53] Shenglong Wang, Sijia Hu, Erika P Brown, Matthew A Nakatsuka, Jiafei Zhao, Mingjun Yang, Yongchen Song, and Carolyn A Koh. High pressure micromechanical force measurements of the effects of surface corrosion and

salinity on ch 4/c 2 h 6 hydrate particle–surface interactions. *Physical Chemistry Chemical Physics*, 19(20):13307–13315, 2017.

[54] G Aspenes, LE Dieker, ZM Aman, S Høiland, AK Sum, CA Koh, and ED Sloan. Adhesion force between cyclopentane hydrates and solid surface materials. *Journal of colloid and interface science*, 343(2):529–536, 2010.

[55] Bo Ram Lee, Carolyn A Koh, and Amadeu K Sum. Mechanism of cohesive forces of cyclopentane hydrates with and without thermodynamic inhibitors. *Industrial & Engineering Chemistry Research*, 53(47):18189–18193, 2014.

[56] D Lippmann, D Kessel, and I Rahimian. Gas hydrate equilibria and kinetics of gas/oil/water mixtures. *Annals of the New York Academy of Sciences*, 715(1):525–527, 1994.

[57] Michael Kauffeld, Masahiro Kawaji, and Peter W Egolf. Handbook on ice slurries. *International Institute of Refrigeration, Paris*, 359, 2005.

[58] Sijia Hu and Carolyn A Koh. Interfacial properties and mechanisms dominating gas hydrate cohesion and adhesion in liquid and vapor hydrocarbon phases. *Langmuir*, 33(42):11299–11309, 2017.

[59] Charles S Campbell and Christopher E Brennen. Computer simulation of granular shear flows. *Journal of Fluid Mechanics*, 151:167–188, 1985.

[60] Diego B Genovese. Shear rheology of hard-sphere, dispersed, and aggregated suspensions, and filler-matrix composites. *Advances in colloid and interface science*, 171:1–16, 2012.

[61] Amit Ahuja, Genti Zylyftari, and Jeffrey F Morris. Yield stress measurements of cyclopentane hydrate slurry. *Journal of Non-Newtonian Fluid Mechanics*, 220:116–125, 2015.

[62] Lin Ding, Bohui Shi, Xiaofang Lv, Yang Liu, Haihao Wu, Wei Wang, and Jing Gong. Investigation of natural gas hydrate slurry flow properties and flow patterns using a high pressure flow loop. *Chemical Engineering Science*, 146:199–206, 2016.

[63] Govind A Hegde, Amadeu K Sum, Thomas J Danielson, et al. Multiphase flow modeling for gas hydrates in flow assurance. In *Offshore Technology Conference*. Offshore Technology Conference, 2015.

[64] Jinkyu Yang, Claudio Silvestro, Devvrath Khatri, Luigi De Nardo, and Chiara Daraio. Interaction of highly nonlinear solitary waves with linear elastic media. *Physical Review E*, 83(4):046606, 2011.

[65] Gilson Lomboy, Sriram Sundararajan, Kejin Wang, and Shankar Subramaniam. A test method for determining adhesion forces and hamaker constants of cementitious materials using atomic force microscopy. *Cement and Concrete Research*, 41(11):1157–1166, 2011.

[66] Anthony J Kinloch. *Adhesion and adhesives: science and technology*. Springer Science & Business Media, 2012.

[67] Anakkavur Thattai Santhanam and YP Gupta. Cleavage surface energy of calcite. In *International Journal of Rock Mechanics and Mining Sciences & Geomechanics Abstracts*, volume 5, pages 253–259. Elsevier, 1968.

[68] SR Gough and DW Davidson. Composition of tetrahydrofuran hydrate and the effect of pressure on the decomposition. *Canadian Journal of Chemistry*, 49(16):2691–2699, 1971.

[69] Heath Henley, Edward Thomas, and Angelo Lucia. Density and phase equilibrium for ice and structure i hydrates using the gibbs–helmholtz constrained equation of state. *Chemical Engineering Research and Design*, 92(12):2977–2991, 2014.

[70] Hossein Sojoudi, Matthew R Walsh, Karen K Gleason, and Gareth H McKinley. Investigation into the formation and adhesion of cyclopentane hydrates on mechanically robust vapor-deposited polymeric coatings. *Langmuir*, 31(22):6186–6196, 2015.

[71] T Mori and YH Mori. Characterization of gas hydrate formation in direct-contact cool storage process. *International journal of refrigeration*, 12(5):259–265, 1989.

[72] FP Bowden. Friction on snow and ice. *Proceedings of the Royal Society of London. Series A, Mathematical and Physical Sciences*, 217(1131):462–478, 1953.

[73] Sergiy Sukhorukov. Ice-ice and ice-steel friction in field and in laboratory. 2013.